

# Ad Astra: Simultaneous Tracking and Navigation with Megaconstellation LEO Satellites

Zaher M. Kassas, Nadim Khairallah, and Sharbel Kozhaya

**Abstract**—A framework to exploit megaconstellation low Earth orbit (LEO) satellite signals of opportunity for navigation is developed. This framework, termed simultaneous tracking and navigation (STAN), estimates the navigating vehicle's states simultaneously with the states of orbiting LEO satellites. STAN employs a cognitive receiver that exploits megaconstellation LEO satellite downlink signals to produce navigation observables: pseudorange, Doppler, and/or carrier phase. These observables are fused through an extended Kalman filter (EKF) to aid the vehicle's inertial navigation system (INS) in a tightly coupled fashion. Simulation results are presented demonstrating the efficacy of the STAN framework. These simulations assumed the aerial vehicle to be equipped with an altimeter and a tactical-grade inertial measurement unit (IMU), navigating for 15.43 km in 300 seconds, in which GNSS signals were only available for the first 60 seconds. It is demonstrated that the final three-dimensional (3-D) position error and position root mean squared error (RMSE) of a typical tightly-coupled GNSS-aided INS grows to 1,536 m and 897 m, respectively. In contrast, the STAN framework with 77 LEO satellites (resembling Orbcomm, Iridium NEXT, and Starlink constellations) achieved a final 3-D position error and position RMSE of 15.2 m and 7.3 m, respectively with pseudorange measurements, and 37.1 m and 10.6 m, respectively with Doppler measurements. In addition, the first multi-constellation LEO navigation experimental results of their kind are presented of a ground vehicle traversing 4.15 km in 150 seconds, in which GNSS signals were only available for the first 80 seconds. It is shown that while the final 3-D position error of the vehicle's GNSS-aided INS with a tactical-grade IMU and an altimeter grew to 472.7 m and the 3-D position RMSE grew to 118.5 m; in contrast, the final 3-D position error and position RMSE of the STAN framework with received signals from 2 Orbcomm, 1 Iridium NEXT, and 3 Starlink LEO satellites were 27.1 m and 18.4 m, respectively.

**Keywords**—LEO, megaconstellation, navigation, INS, GNSS.

## I. INTRODUCTION

We are witnessing a space renaissance. An ambitious image of an Earth connected through a web woven from low Earth orbit (LEO) satellites is taking the world by storm, promising high-resolution images; remote sensing; and global, high-availability, high-bandwidth, and low-latency Internet. Older LEO constellations; like Orbcomm, Iridium, and Globalstar;

This work was supported in part by the Office of Naval Research (ONR) under Grant N00014-19-1-2511, in part by the Air Force Office of Scientific Research (AFOSR) under Grant FA9550-22-1-0476, in part by the National Science Foundation (NSF) under Grant 1929965, and in part by the U.S. Department of Transportation (USDOT) under Grant 69A3552047138 for the CARMEN University Transportation Center (UTC).

Z. Kassas and S. Kozhaya are with Department of Electrical and Computer Engineering at The Ohio State University, Columbus, OH 43210, USA. N. Khairallah is with SpaceX, Mountain View, CA 94043, USA. (Corresponding author: Z. Kassas, email: zkassas@ieee.org).

are welcoming a new wave of thousands of broadband megaconstellations, funded by major technology giants, such as SpaceX, Amazon, among others [1]. Fig. 1 shows some of the existing and future LEO megaconstellations that will blanket the Earth. These megaconstellations of LEO satellites will shower the Earth with a plethora of signals of opportunity, diverse in frequency and direction [2] (see Table I). These signals could be exploited for positioning, navigation, and timing in the inevitable event that global navigation satellite system (GNSS) signals become unavailable [3] (e.g., in deep urban canyons, under dense foliage, during unintentional interference, and intentional jamming) or untrustworthy (e.g., under malicious spoofing attacks).

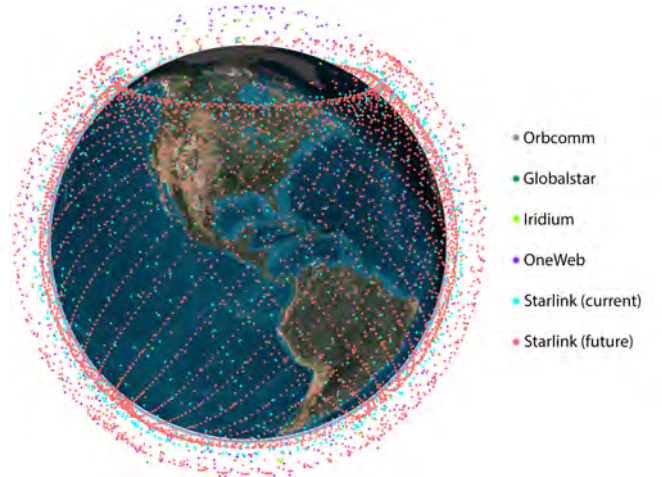


Fig. 1. Existing and future LEO satellite constellations

TABLE I  
SOME EXISTING AND FUTURE LEO SATELLITE CONSTELLATIONS

	System	Number of satellites	Frequency band
Existing	Orbcomm	36	VHF
	Globalstar	48	S and C
	Iridium NEXT	66	L and Ka
	Boeing	147	V and Ka
Future	SpaceMobile	243	Ka and V
	OneWeb	882	Ku and Ka
	Telesat	1,671	Ku and Ka
	Kuiper (Amazon)	3,236	Ku and Ka
	Starlink (SpaceX)	11,943	Ku, Ka, and V

The concept of large LEO satellite constellations is not new; however, recent developments in satellite technology,

reduction in launch costs and commercialization of LEO megaconstellations, have been key enablers to realize LEO satellite megaconstellations. This rapidly developing frontier is attracting many players, from government and defense agencies, to private corporations, to international competitors.

The promise of utilizing LEO satellites for navigation has been the subject of numerous recent studies [4]–[21]. While some studies call for tailoring the transmission protocol to support navigation capabilities [22]–[27], other studies propose to exploit the transmitted signals for navigation in an opportunistic fashion [28]–[37]. The former studies allow for simpler receiver architectures and navigation algorithms. However, they require significant investment in satellite infrastructure and spectrum allocation, the cost of which private corporations; such as OneWeb, SpaceX, Amazon, Telesat, Boeing, among others; which are planning to aggregately launch tens of thousands of satellites into LEO may not be willing to pay. Even if these corporations agree to that additional cost, there will be no guarantees that they would not charge for “extra navigation services.” As such, exploiting LEO satellite signals opportunistically for navigation becomes the more viable approach.

To address the limitations and vulnerabilities of GNSS, opportunistic navigation has received significant attention over the past decade or so. Opportunistic navigation is a paradigm that relies on exploiting ambient radio signal of opportunity for positioning, navigation, and timing [38]. Besides LEO satellite signals, other signals of opportunity include AM/FM radio [39], [40], digital television [41], [42], and cellular [43]–[47], with the latter yielding submeter-accurate navigation on unmanned aerial vehicles [48] and meter-level navigation on ground vehicles [49].

This article considers *opportunistic* navigation with megaconstellation LEO satellites. In other words, it does not consider LEO constellations specifically designed for navigation purposes [50] (commonly referred to “cooperative” satellites) but instead, it focuses on exploiting LEO satellite signals of opportunity which are “non-cooperative,” i.e., those with minimal and imperfect knowledge about their signals and ephemerides. Nevertheless, opportunistic navigation with “non-cooperative” satellites poses numerous intriguing scientific and design questions, some of which are addressed in this article.

It is worth noting that while LEO constellations with dedicated navigation services could offer certain quality of service guarantees (e.g., accuracy, coverage, and integrity), they suffer from certain drawbacks when compared to opportunistic approaches: (1) the user’s privacy could be compromised since the user’s location is revealed to the provider (upon communicating with the satellite and/or dedicated ground stations), (2) navigation services are limited only to paying subscribers and from a particular LEO constellation, (3) ambient LEO signals transmitted by other constellations providers are not exploited, and (4) considerable cost is required to launch and maintain these dedicated constellations.

This article presents an opportunistic navigation framework, termed STAN: simultaneous tracking and navigation, which addresses the challenges associated with navigating with LEO satellites’ signals of opportunity whose states are minimally

known. STAN estimates the LEO satellites’ states simultaneously with the vehicle’s states. STAN, originally proposed in [5], is analogous to radio simultaneous localization and mapping (radio SLAM) [51], which considered *stationary* terrestrial signals of opportunity transmitters; with the added complexity of tracking the *mobile* LEO satellites’ states. STAN utilizes a LEO receiver to extract pseudorange, Doppler, and/or carrier phase observables from LEO signals, which are used to aid the vehicle-mounted inertial navigation system (INS) in a tightly-coupled fashion. The efficacy of the STAN framework is illustrated via high fidelity numerical simulations. These simulations assumed an aerial vehicle to be equipped with an altimeter and a tactical-grade inertial measurement unit (IMU), navigating for 15.43 km in 300 seconds, in which GNSS signals were only available for the first 60 seconds. It is demonstrated that the final three-dimensional (3-D) position error and position root mean squared error (RMSE) of a tightly-coupled GNSS-aided INS grew to 1,536 m and 897 m, respectively. In contrast, the STAN framework with 77 LEO satellites (resembling Orbcomm, Iridium NEXT, and Starlink constellations) achieved a final 3-D position error and position RMSE of 15.2 m and 7.3 m, respectively, with pseudorange measurements; and 7.1 m and 10.6 m, respectively, with Doppler measurements. The first multi-constellation LEO navigation experimental results of their kind are presented of a ground vehicle traversing 4.15 km in 150 seconds, in which GNSS signals were only available for the first 80 seconds. It is shown that while the final 3-D position error and position RMSE of the vehicle’s GNSS-aided INS with a tactical-grade IMU and an altimeter was 472.7 m and 118.5 m, respectively; in contrast, the LEO-aided INS STAN framework with signals from 2 Orbcomm, 1 Iridium NEXT, and 3 Starlink LEO satellites achieved a final 3-D position error and position RMSE of 27.1 m and 18.4 m, respectively.

The rest of the paper is organized as follows. Section II overviews the opportunities and challenges associated with navigation with megaconstellation LEO satellites. Section III describes the STAN framework. Section IV presents simulation results to study the efficacy of aerial vehicle navigation with STAN using simulated Starlink, Orbcomm, and Iridium NEXT LEO satellites. Section V shows experimental results of a ground vehicle navigating via the proposed STAN framework with carrier phase measurements from Orbcomm and Doppler measurements from Starlink and Iridium NEXT LEO satellites. Section VI gives concluding remarks.

## II. NAVIGATION WITH MEGACONSTELLATION LEO SATELLITES: OPPORTUNITIES AND CHALLENGES

LEO satellites possess desirable attributes for navigation [52], [53]:

- LEO satellites are around twenty-times closer to Earth compared to GNSS satellites that reside in medium-Earth orbit (MEO), which results in less spreading loss, improving the carrier-to-noise ratio ( $C/N_0$ ) by about 30 dB (the reader is referred to Fig. 2 in [54], which shows the spreading loss (dB) and slant range (km) as a function of altitude for LEO, MEO, and geostationary orbit (GSO) satellites).

- LEO satellites orbit the Earth at much faster rates compared to GNSS satellites, making (i) LEO satellites' Doppler measurements attractive to exploit, whether in a standalone fashion or fused with pseudorange measurements [55] or (ii) enabling receiver positioning with as few as one satellite within a relatively short period of time [56].
- LEO megaconstellations will shower Earth with signals that span a wide swath of frequency spectrum (see Table I), which improves robustness to interference and cyberattacks.
- LEO megaconstellation satellites will provide virtually a blanket cover around the globe. The sheer number of LEO satellites will compensate for their smaller footprint compared to GNSS satellites. Essentially, with planned megaconstellations, each spot on Earth could have many times more visible LEO satellites than GNSS. This would offset the requirement that one needs about ten-times more LEO satellites than those in MEO to get the same geometric dilution of precision (GDOP). These are not ungrounded promises. As of early 2022, SpaceX has launched over 2,000 Starlink satellites into LEO, with the total being projected to be up to 42,000 satellites, nearly 12,000 of which are already approved by the Federal Communications Commission (FCC).

However, there is no such thing as a free lunch. A multitude of challenges must be addressed to be able to exploit "non-cooperative" LEO satellite signals in an opportunistic fashion. First, since these LEO satellites are not designed for navigation purposes, they do not necessarily transmit their satellites' ephemerides and in occasions that they do [57], non-subscribers might not have access to such data. The position and velocity of a satellite can be parametrized by its Keplerian elements: eccentricity, semi-major axis, inclination, longitude of the ascending node, argument of periapsis, and true anomaly. With time, these orbital elements will drift from their nominal values due to several perturbing forces acting on the LEO satellite. In contrast to GNSS, where corrections to the orbital elements and clock errors are periodically transmitted to the receiver in the navigation message, this may not be the case for LEO satellites; in which case they must be estimated. An orbit propagator and initialization scheme should be selected to carry out this estimation problem [58]. Orbit propagators consist of equations of motion governed by force models, which fall into two main categories: analytical and numerical [59], [60]. They differ by trading-off accuracy with computational complexity. On one hand, in order to achieve a computationally efficient analytical solution, analytical propagators reduce model fidelity, which in turn degrades the propagation accuracy. On the other hand, numerical approaches achieve higher accuracy by performing costly numerical integrations of complicated force models. For instance, the LEO analytical propagator known as simplified general perturbations 4 (SGP4), uses two-line element (TLE) files that contain orbital elements and corrective terms to initialize and propagate the position and velocity of a satellite [61]. TLEs are produced daily by the

North American Aerospace Defense Command (NORAD) to support the on-going usage of SGP4 as an orbit determination method. The information in TLE files can be used to initialize any SGP model to propagate a satellite in its orbit. However, the simplified models of perturbing forces, which include non-uniform Earth gravitational field, atmospheric drag, solar radiation pressure, third-body gravitational forces (e.g., gravity of the Moon and Sun), and general relativity, cause errors in a propagated satellite orbit of around 3–10 km, 24-hours after a TLE is produced [62]. In contrast, numerical propagators, also known as precise orbit determination (POD) methods, yield accurate ephemerides with errors on the order of tens-of-meters, in the radial, along-track, and cross-track directions for a satellite, with more error occurring in the along-track direction [63]. Unlike SGP propagators, POD propagators do not have a TLE-equivalent initialization file that is publicly available. It is worth noting that GNSS-aided orbital filtering [64]–[66] provides a decimeter-level and millimeter-per-second accuracy of LEO satellite position and velocity, respectively. However, a ground receiver might not have access to the navigation solution of GNSS receivers onboard the LEO satellite, which is the rationale behind the opportunistic navigation paradigm. Recently, machine learning approaches have shown great promise for improved orbit propagation [67]–[70].

Second, unlike GNSS satellites, LEO satellites are not necessarily equipped with highly stable atomic clocks, nor they are as tightly synchronized. The stability of LEO satellites' clocks and their synchronicity are unknown. In contrast to GNSS, where the satellites' clock errors are periodically transmitted to the receiver in the navigation message, this may not be the case for LEO satellites.

Finally, LEO satellites are owned and operated by private entities, which adopt proprietary transmission protocols; making their signals "mysterious" for non-subscribers. As such, to exploit these signals, specialized receivers that are capable of extracting navigation observables must be designed.

This proposed STAN framework presented in this article addresses the aforementioned challenges. STAN considers a navigating vehicle equipped with a cognitive software-defined LEO satellite receiver (e.g., [71], [72]), which is capable of producing navigation observables: pseudorange, Doppler, and/or carrier phase from received LEO satellite signals. These observables are used to aid the vehicle-mounted INS in a tightly coupled fashion via an extended Kalman filter (EKF), which estimates the LEO satellites' states (position and velocity) simultaneously with the vehicle's INS' states (orientation, position, velocity, and gyroscope and accelerometer biases), as well as the clock bias and drift difference between the vehicle-mounted receiver and each of the LEO satellites.

### III. STAN: SIMULTANEOUS TRACKING AND NAVIGATION WITH LEO SATELLITE SIGNALS

Unlike GNSS satellites that periodically transmit accurate information about their positions and clock errors, such information about LEO satellites is generally unavailable. The STAN framework addresses this by extracting pseudorange, Doppler, and/or carrier phase measurements from LEO satellite to aid the vehicle's INS, while simultaneously tracking



where  $\mu$  is Earth's standard gravitational parameter,  $P_n$  is a Legendre polynomial with harmonic  $n$ ,  $J_n$  is the  $n$ -th zonal coefficient,  $R_E$  is the mean radius of the Earth,  $\sin(\theta_l) = z_{\text{leo}_l} / \|\mathbf{r}_{\text{leo}_l}\|$ , and  $N = \infty$ . Since the acceleration due to the  $J_2$  coefficient is approximately three orders of magnitude greater than the acceleration due to the other zonal coefficients modeling Earth's oblateness, the perturbation due to non-uniform gravity will be approximated by using only the term corresponding to  $J_2$ . Taking the partial derivative of (8) with respect to the components of  $\mathbf{r}_{\text{leo}_l}$  with  $N \equiv 2$  gives the components of  $\mathbf{a}_{\text{grav}_l} = [\ddot{x}_{\text{grav}_l}, \ddot{y}_{\text{grav}_l}, \ddot{z}_{\text{grav}_l}]^T$  as

$$\begin{aligned}\ddot{x}_{\text{grav}_l} &= -\frac{\mu x_{\text{leo}_l}}{\|\mathbf{r}_{\text{leo}_l}\|^3} \left[ 1 + J_2 \frac{3}{2} \left( \frac{R_E}{\|\mathbf{r}_{\text{leo}_l}\|} \right)^2 \left( 1 - 5 \frac{z_{\text{leo}_l}^2}{\|\mathbf{r}_{\text{leo}_l}\|^2} \right) \right], \\ \ddot{y}_{\text{grav}_l} &= -\frac{\mu y_{\text{leo}_l}}{\|\mathbf{r}_{\text{leo}_l}\|^3} \left[ 1 + J_2 \frac{3}{2} \left( \frac{R_E}{\|\mathbf{r}_{\text{leo}_l}\|} \right)^2 \left( 1 - 5 \frac{z_{\text{leo}_l}^2}{\|\mathbf{r}_{\text{leo}_l}\|^2} \right) \right], \\ \ddot{z}_{\text{grav}_l} &= -\frac{\mu z_{\text{leo}_l}}{\|\mathbf{r}_{\text{leo}_l}\|^3} \left[ 1 + J_2 \frac{3}{2} \left( \frac{R_E}{\|\mathbf{r}_{\text{leo}_l}\|} \right)^2 \left( 3 - 5 \frac{z_{\text{leo}_l}^2}{\|\mathbf{r}_{\text{leo}_l}\|^2} \right) \right].\end{aligned}\quad (9)$$

Further analysis comparing different LEO orbital models can be found in [77], [78].

### C. Clock Dynamics Model

The receiver's and LEO satellites' clock error state dynamics are assumed evolve according to [79]

$$\begin{aligned}\mathbf{x}_{\text{clk},i}(k+1) &= \mathbf{F}_{\text{clk}} \mathbf{x}_{\text{clk},i}(k) + \mathbf{w}_{\text{clk},i}(k), \\ \mathbf{x}_{\text{clk},i} &\triangleq [c\delta t_i, c\dot{\delta t}_i]^T, \quad \mathbf{F}_{\text{clk}} = \begin{bmatrix} 1 & T \\ 0 & 1 \end{bmatrix},\end{aligned}\quad (10)$$

where  $i = \{r, \text{leo}_l\}$ ,  $\delta t_i$  is the clock bias,  $\dot{\delta t}_i$  is the clock drift,  $c$  is the speed of light,  $T$  is the constant sampling interval, and  $\mathbf{w}_{\text{clk},i}$  is the process noise, which is modeled as a discrete-time white noise sequence with covariance

$$\mathbf{Q}_{\text{clk},i} = c^2 \cdot \begin{bmatrix} S_{\bar{w}_{\delta t_i}} T + S_{\bar{w}_{\dot{\delta t}_i}} \frac{T^3}{3} & S_{\bar{w}_{\delta t_i}} \frac{T^2}{2} \\ S_{\bar{w}_{\delta t_i}} \frac{T^2}{2} & S_{\bar{w}_{\dot{\delta t}_i}} T \end{bmatrix}, \quad (11)$$

The terms  $S_{\bar{w}_{\delta t_i}}$  and  $S_{\bar{w}_{\dot{\delta t}_i}}$  are the clock bias and drift process noise PSDs, respectively, which can be related to the power-law coefficients,  $\{h_{\alpha_i}\}_{\alpha_i=-2}^2$ , which have been shown through laboratory experiments to characterize the power spectral density of the fractional frequency deviation of an oscillator from nominal frequency according to  $S_{\bar{w}_{\delta t_i}} \approx \frac{h_{0,i}}{2}$  and  $S_{\bar{w}_{\dot{\delta t}_i}} \approx 2\pi^2 h_{-2,i}$  [80]. The receiver's and LEO satellites' process noise covariances  $\mathbf{Q}_{\text{clk}_r}$  and  $\mathbf{Q}_{\text{clk}_{\text{leo}}}$  are calculated from (11) using the PSDs associated with the receiver's and LEO satellites' oscillator quality, respectively.

The dynamics of the difference between the receiver's and LEO satellites' clock error states is given by

$$\Delta \mathbf{x}_{\text{clk}}(k+1) = \mathbf{F}_{\Delta \text{clk}} \Delta \mathbf{x}_{\text{clk}}(k) + \Delta \mathbf{w}_{\text{clk}}(k), \quad (12)$$

$$\begin{aligned}\Delta \mathbf{x}_{\text{clk}} &\triangleq [c\Delta \delta t_{\text{leo}_1}, c\Delta \dot{\delta t}_{\text{leo}_1}, \dots, c\Delta \delta t_{\text{leo}_L}, c\Delta \dot{\delta t}_{\text{leo}_L}]^T, \\ c\Delta \delta t_{\text{leo}_l} &\triangleq c \cdot [\delta t_r - \delta t_{\text{leo}_l}], \quad c\Delta \dot{\delta t}_{\text{leo}_l} \triangleq c \cdot [\dot{\delta t}_r - \dot{\delta t}_{\text{leo}_l}],\end{aligned}$$

where  $\mathbf{F}_{\Delta \text{clk}} = \mathbf{I}_{L \times L} \otimes \mathbf{F}_{\text{clk}}$ , with  $\otimes$  denoting the Kronecker product, and  $\Delta \mathbf{w}_{\text{clk}}$  is the process noise which has a covariance  $\mathbf{Q}_{\Delta \text{clk}}$  that encapsulates the correlation between entries of  $\Delta \mathbf{x}_{\text{clk}}$  resulting from the common process noise of the receiver clock states. Assuming the LEO satellites to be equipped with identical oscillators,  $\mathbf{Q}_{\Delta \text{clk}}$  simplifies to

$$\mathbf{Q}_{\Delta \text{clk}} = \mathbb{1}_{L \times L} \otimes \mathbf{Q}_{\text{clk}_r} + \mathbf{I}_{L \times L} \otimes \mathbf{Q}_{\text{clk}_{\text{leo}}},$$

where  $\mathbb{1}_{L \times L}$  is the  $L \times L$  matrix with all entries equal to 1 and  $\mathbf{I}_{L \times L}$  is the  $L \times L$  identity matrix.

### D. Measurement Models

It is assumed that the vehicle is equipped with a receiver [81] capable of extracting navigation observables (pseudorange [25], [82], [83]; Doppler [29], [37], [71], [72], [84]; and/or carrier phase [7], [85]) from LEO satellite signals. It is worth mentioning that the amenability of extracting certain navigation observables varies among LEO constellations. This has to do with the sophistication of their transmitted signals and the amount of publicly disclosed information about their signals. For instance, while it is less challenging to design a receiver capable of producing Doppler measurements from Orbcomm satellites or pseudorange measurements from Globalstar satellites, it is much more involved to design a receiver capable of producing pseudorange measurements from Starlink satellites. The recently established paradigm, termed cognitive opportunistic navigation, is showing promise in producing navigation observables from minimally known LEO satellite signals [83], [86], [87]. While the receiver design details is beyond the scope of this article, the focus herein is to study the navigation potential with different navigation observables via the STAN framework. Models of the measurements produced by the vehicle-mounted LEO receiver, relating the vehicle's states to the LEO satellites' states are presented next.

1) *Pseudorange Measurement Model*: A LEO receiver extracts pseudorange measurements  $\rho$  from LEO satellites by estimating the time-of-arrival. The pseudorange  $\rho_l$  from the  $l$ -th LEO satellite at time-step  $k$ , which represents discrete-time instant  $t_k = kT + t_0$  for an initial time  $t_0$ , is modeled as

$$\begin{aligned}\rho_l(k) &= \|\mathbf{r}_r(k) - \mathbf{r}_{\text{leo}_l}(k'_l)\|_2 + c \cdot [\delta t_r(k) - \delta t_{\text{leo}_l}(k'_l)] \\ &\quad + c\delta t_{\text{iono}_l}(k) + c\delta t_{\text{tropo}_l}(k) + v_{\rho_l}(k), \\ l &= 1, \dots, L \quad k = 1, 2, \dots\end{aligned}\quad (13)$$

where  $k'_l$  represents discrete-time at  $t_{k'} = kT + t_0 - \delta t_{\text{TOF}_l}$ , with  $\delta t_{\text{TOF}_l}$  being the true time-of-flight of the signal from the  $l$ -th LEO satellite;  $\mathbf{r}_r$  and  $\mathbf{r}_{\text{leo}_l}$  are the receiver's and  $l$ -th LEO satellite's 3-D position vectors expressed in the same reference frame, respectively;  $\delta t_r$  and  $\delta t_{\text{leo}_l}$  are the receiver's and  $l$ -th LEO satellite transmitter's clock biases, respectively;  $\delta t_{\text{iono}_l}$  and  $\delta t_{\text{tropo}_l}$  are the ionospheric and tropospheric delays, respectively, affecting the  $l$ -th LEO satellite's signal;  $L$  is the total number of visible LEO satellites; and  $v_{\rho_l}$  is the pseudorange measurement noise, which is modeled as a white Gaussian random sequence with variance  $\sigma_{\rho,l}^2$ .

2) *Doppler Measurement Model*: A LEO receiver extracts Doppler frequency measurements  $f_D$  from LEO satellites by subtracting the nominal carrier frequency from the received signal frequency. A pseudorange rate measurement  $\dot{\rho}$  can be obtained from

$$\dot{\rho} = -\frac{c}{f_c} f_D, \quad (14)$$

where  $f_c$  is the carrier frequency.

A pseudorange rate measurement  $\dot{\rho}$  from the  $l$ -th LEO satellite is modeled by

$$\begin{aligned} \dot{\rho}_l(k) = & [\dot{\mathbf{r}}_r(k) - \dot{\mathbf{r}}_{\text{leo}_l}(k'_l)]^T \frac{[\mathbf{r}_r(k) - \mathbf{r}_{\text{leo}_l}(k'_l)]}{\|\mathbf{r}_r(k) - \mathbf{r}_{\text{leo}_l}(k'_l)\|_2} + \\ & c \cdot [\dot{\delta}t_r(k) - \dot{\delta}t_{\text{leo}_l}(k'_l)] + c\dot{\delta}t_{\text{iono}_l}(k) + c\dot{\delta}t_{\text{tropo}_l}(k) + v_{\dot{\rho}_l}(k), \end{aligned} \quad (15)$$

where  $\dot{\mathbf{r}}_r$  and  $\dot{\mathbf{r}}_{\text{leo}_l}$  are the receiver's and  $l$ -th LEO satellite's 3-D velocity vectors expressed in the same reference frame, respectively;  $\dot{\delta}t_r$  and  $\dot{\delta}t_{\text{leo}_l}$  are the receiver's and  $l$ -th LEO satellite's transmitter clock drifts, respectively;  $\dot{\delta}t_{\text{iono}_l}$  and  $\dot{\delta}t_{\text{tropo}_l}$  are the ionospheric and tropospheric delay rates, respectively, affecting the  $l$ -th LEO satellite's signal; and  $v_{\dot{\rho}_l}$  is the pseudorange rate measurement noise, which is modeled as a white Gaussian random sequence with variance  $\sigma_{\dot{\rho}_l}^2$ .

3) *Carrier Phase Measurement Model*: The continuous-time carrier phase observable can be obtained by integrating the Doppler measurement over time [88]. The carrier phase measurement (expressed in meters) made by the receiver on the  $l$ -th LEO satellite can be modeled in discrete-time as

$$\begin{aligned} \phi_l(k) = & \|\mathbf{r}_r(k) - \mathbf{r}_{\text{leo}_l}(k'_l)\|_2 + c[\delta t_r(k) - \delta t_{\text{leo}_l}(k'_l)] + \lambda_l N_l \\ & + c\delta t_{\text{iono},l}(k) + c\delta t_{\text{tropo},l}(k) + v_l(k), \end{aligned} \quad (16)$$

where  $\lambda_l$  is the wavelength of the carrier signal transmitted by the  $l$ -th LEO satellite,  $N_l$  is the carrier phase ambiguity of the  $l$ -th LEO satellite carrier phase measurement, and  $v_l$  is the measurement noise, which is modeled as a zero-mean white Gaussian random sequence with variance  $\sigma_{\phi_l}^2$ .

### E. Filter Formulation

This section formulates the EKF adopted in the STAN framework to fuse navigation observables extracted opportunistically from the LEO satellites' signals with the IMU measurements, to aid the vehicle-mounted INS.

1) *EKF State Vector*: The EKF state vector is given by

$$\begin{aligned} \mathbf{x} &= [\mathbf{x}_r^T, \mathbf{x}_{\text{leo}_1}^T, \dots, \mathbf{x}_{\text{leo}_L}^T]^T \\ \mathbf{x}_r &= [{}^b_g \bar{\mathbf{q}}^T, \mathbf{r}_r^T, \dot{\mathbf{r}}_r^T, \mathbf{b}_g^T, \mathbf{b}_a^T]^T \\ \mathbf{x}_{\text{leo}_l} &= [\mathbf{r}_{\text{leo}_l}^T, \dot{\mathbf{r}}_{\text{leo}_l}^T, c\Delta\delta t_{\text{leo}_l}, c\Delta\dot{\delta}t_{\text{leo}_l}]^T, \end{aligned}$$

where  $\mathbf{x}_r$  is the vehicle's state vector, composed of  ${}^b_g \bar{\mathbf{q}} \triangleq [{}^b_g \mathbf{q}^T, {}^b_g q]^T$ , which is a 4-D unit quaternion representing the orientation of  $\{b\}$  fixed at the IMU with respect to  $\{g\}$ ,  $\mathbf{r}_r$  and  $\dot{\mathbf{r}}_r$  are the 3-D position and velocity of the vehicle expressed in  $\{g\}$ , and  $\mathbf{b}_g$  and  $\mathbf{b}_a$  are 3-D biases of the IMU's gyroscopes and accelerometers, respectively, expressed in  $\{b\}$ . Quaternions were chosen to represent the orientation of the vehicle with

respect to  $\{g\}$ , since they offer minimal attitude representation without suffering from the singularity of other mathematical attitude representations (e.g., Euler angles). However, since the 4-D quaternion is an overdetermined representation of attitude, the estimation error covariance associated with orientation is represented by three-by-three matrix corresponding to a three-axis error angle vector to prevent degeneracy. The vector  $\mathbf{x}_{\text{leo}_l}$  is the  $l$ -th LEO satellite state vector, composed of the LEO satellite's position  $\mathbf{r}_{\text{leo}_l}$  and velocity  $\dot{\mathbf{r}}_{\text{leo}_l}$  vectors, expressed in the ECI frame, and the difference between the receiver's and  $l$ -th LEO satellite's clock bias  $c\Delta\delta t_{\text{leo}_l}$  and drift  $c\Delta\dot{\delta}t_{\text{leo}_l}$ .

2) *EKF Prediction*: The EKF prediction step produces an estimate  $\hat{\mathbf{x}}(k|j) \triangleq \mathbb{E}[\mathbf{x}(k)|\mathbf{Z}^j]$  of  $\mathbf{x}(k)$ , and an associated estimation error covariance  $\mathbf{P}_x(k|j)$ , where  $\mathbb{E}[\cdot|\cdot]$  denotes the conditional expectation,  $\mathbf{Z}^j \triangleq \{\mathbf{z}(i)\}_{i=1}^j$  is the set of measurements available up to and including time index  $j$ , and  $k > j$ . The measurements  $\mathbf{z}$  are the pseudorange, Doppler, and/or carrier phase measurements discussed in Subsection III-D.

The IMU measurements (3) and (4) are processed through a vector-valued function of strapdown INS equations in  $\{g\}$  that discretize (1) and (2) to obtain [51], [89]

$$\hat{\mathbf{x}}_r(k+1|j) = \mathbf{f}_{\text{ins}}^{\{g\}}[\hat{\mathbf{x}}_r(k|j), \boldsymbol{\omega}_{\text{imu}}(k), \mathbf{a}_{\text{imu}}(k)],$$

where the gyroscope and accelerometer bias predictions  $\hat{\mathbf{b}}_g(k+1|j)$  and  $\hat{\mathbf{b}}_a(k+1|j)$  follow from (5) and (6), respectively. The INS mechanization equations are performed with the ECI frame as  $\{g\}$  since the LEO satellites' position and velocity states are also expressed in ECI. This facilitates the EKF update step as the receiver's and LEO satellites' position and velocity states and the corresponding estimation error covariances are all expressed in the same reference frame in this case. The ECI strapdown mechanization equations are presented in Appendix A and their linearization to propagate the estimation error covariance are detailed in Appendix B. The prediction of the differenced clock states between the receiver and the LEO satellite transmitter follow from (12). The prediction of the LEO satellites' position and velocity is performed by numerical integration of (7) using the gravitational accelerations obtained from the two-body model with  $J_2$  perturbations in (9).

3) *EKF Update*: The vehicle-mounted receiver makes pseudorange  $\rho_{\text{leo}}$ , Doppler  $f_{D,\text{leo}}$ , and/or carrier phase  $\phi_{\text{leo}}$  measurements whose models are discussed in Subsection III-D. The measurement vector  $\mathbf{z}$  processed by the EKF update step is defined by stacking all the extracted LEO navigation observables. In the tracking mode of STAN, GNSS pseudoranges  $\rho_{\text{gnss}}$  are processed by the receiver to produce a GNSS-only navigation solution, which gets augmented into  $\mathbf{z}$ . In the STAN mode, only LEO navigation observables in  $\mathbf{z}$  are processed in the EKF update step. The EKF update step produces an estimate  $\hat{\mathbf{x}}(k|k)$  and an associated posterior estimation error covariance  $\mathbf{P}_x(k|k)$ . Details on the EKF update equations are given in Appendix C.

It is worth noting that tight coupling of GNSS pseudoranges  $\rho_{\text{gnss}}$  with the INS can be readily implemented into the STAN framework with little modification to the EKF formulation. First, in the tracking mode, the EKF state vector is augmented

to include the receiver's clock bias and drift states, in which case the LEO satellites' clock error states can also be estimated individually (i.e., instead of the differenced clock error states). The measurement vector  $z$  is also augmented by including the GNSS pseudoranges  $\rho_{\text{gnss}}$  to perform tight coupling during the EKF update. Second, in the STAN mode, a transformation is performed on the estimated states and associated error covariance to form the differenced clock error states, thus preventing stochastic unobservability issues [90]. More details on the GNSS tight coupling implementation can be found in [51], which performed a similar approach in the context of radio SLAM with terrestrial signals of opportunity. It is worth noting that while the receiver's clock process noise covariance  $\mathbf{Q}_{\text{clk},r}$  can be readily found from specification sheets, the satellite's clock process noise covariance  $\mathbf{Q}_{\text{clk},\text{leo}_i}$  is typically unknown, in which case one could adopt either standard off-line filter tuning techniques or online adaptive estimation [91].

**Remark:** The strapdown INS mechanization equations can be performed in any global reference frame instead of ECI with some additional considerations. For the simulations and experimental results of this article, the Earth-centered Earth-fixed (ECEF) frame was used to perform the INS prediction to facilitate the conversion of the receiver's position and velocity estimates to a local East-North-Up (ENU) reference frame. However, before each EKF update, the LEO satellites' states and associated covariances were converted from ECI to ECEF, the STAN update was performed in ECEF using LEO satellite measurements, and then the LEO satellites' states and covariances were converted back to ECI for the next EKF prediction step. The ECI to ECEF and ECI to ECEF conversions were performed by accounting for Earth's rotation, precession and nutation effects, and polar motion.

#### IV. SIMULATION RESULTS

This section presents a glimpse of the future with simulation results illustrating the potential of the STAN framework with existing Orbcomm and Iridium NEXT constellations and the future Starlink megaconstellation.

##### A. Scenario Description

The simulations considered a fixed-wing aerial vehicle with comparable performance to a small private plane with a cruise speed of roughly 50 m/s. The aerial vehicle was equipped with a tactical-grade IMU, an altimeter, and a GNSS receiver. This aerial vehicle fused altimeter measurements and GNSS pseudoranges to aid the onboard INS. The aerial vehicle was also equipped with Starlink, Orbcomm, and Iridium NEXT LEO receivers that produced pseudorange and Doppler measurements from the downlink signals of these constellations' satellites. It is assumed in these simulations that the LEO receivers can extract navigation observables from all LEO satellites above a specified elevation mask, which are referred to as "visible" satellites. The aerial vehicle flew a 300-second trajectory covering 15.43 km, over Irvine, California, USA. The trajectory consisted of a straight climbing segment, followed by a figure-eight pattern, and then a final descent into a straight segment. The aerial vehicle, initially at 1 km altitude,

climbed to an altitude of 1.5 km, where it began executing rolling and yawing maneuvers before descending back down to 1 km in the straight segment.

The state vector  $x$  defined in Subsection III-E1 was estimated by the aerial vehicle. GNSS signals were initially available for the first 60 seconds of the flight, during which the aerial vehicle was in Tracking Mode: altimeter measurements and the navigation solution produced by the GNSS receiver aided the INS in a loosely coupled fashion, while the observables extracted opportunistically from the LEO signals were processed to refine the LEO satellites' ephemeris and estimate the clock error states. The GNSS signals were then fictitiously cut off and the aerial vehicle flew the last 240 seconds of the trajectory in an emulated GNSS-denied environment. Operating now in the STAN mode, the aerial vehicle fused the altimeter measurements with the LEO satellites' observables to aid the INS, while simultaneously tracking the LEO satellites' ephemeris and estimating the clock error states.

##### B. Simulation Setup

This subsection details the simulation environment setup: generation of IMU measurements, LEO satellite trajectories, clock error states, and Doppler and pseudorange measurements.

1) *IMU Measurements:* The aerial vehicle was equipped with a tactical-grade IMU with bias instability and noise density parameters for all axes summarized in Table II. Gyroscope and accelerometer measurements were generated at a rate of 100 Hz along the aerial vehicle trajectory according to (3)-(4). The gyroscope and accelerometer bias instability process noise covariances are expressed as  $\mathbf{Q}_{\text{bg}} = \sigma_{\text{bg}}^2 \mathbf{I}_{3 \times 3}$  and  $\mathbf{Q}_{\text{ba}} = \sigma_{\text{ba}}^2 \mathbf{I}_{3 \times 3}$ , where  $\sigma_{\text{bg}}^2$  and  $\sigma_{\text{ba}}^2$  are computed by squaring the bias instability parameters of Table II, expressed in rad/s and m/s<sup>2</sup>, respectively. The gyroscope and accelerometer measurement noise covariances are expressed as  $\mathbf{Q}_{\text{ng}} = \sigma_{\text{ng}}^2 \mathbf{I}_{3 \times 3}$  and  $\mathbf{Q}_{\text{na}} = \sigma_{\text{na}}^2 \mathbf{I}_{3 \times 3}$ , where  $\sigma_{\text{ng}}^2$  and  $\sigma_{\text{na}}^2$  are computed by first multiplying the noise density parameters of Table II by the square root of the IMU sampling rate and then squaring the resulting quantities expressed in rad/s and m/s<sup>2</sup>, respectively.

TABLE II  
AERIAL VEHICLE'S TACTICAL-GRADE IMU PARAMETERS

	Gyroscope	Accelerometer
Bias Instability	1.5°/hr	100 $\mu\text{g}$
Noise Density	1.5°/hr/ $\sqrt{\text{Hz}}$	110 $\mu\text{g}/\sqrt{\text{Hz}}$

2) *LEO Satellites' Trajectories:* The FCC-approved 12,000-satellite Starlink constellation was simulated using orbital parameters found in the FCC filings. In addition, currently active second-generation Orbcomm satellites and the Iridium NEXT constellation were simulated to take advantage of LEO satellites' geometric and spectral diversities. The LEO satellites' trajectories were obtained through SGP4 propagations of simulated TLEs for the 12,000 Starlink constellation and existing TLEs for Orbcomm and Iridium NEXT constellations.

3) *Clock Errors*: The aerial vehicle was equipped with a high-quality oven-controlled crystal oscillator (OCXO) and the LEO satellites were assumed to have chip-scale atomic clocks (CSACs). The power-law coefficients of these oscillators are given in Table III. The clock bias and drift of the aerial vehicle-mounted LEO receiver and LEO satellite transmitters were simulated according to the models described in Subsection III-C. The values of the aerial vehicle clock error states  $\mathbf{x}_{\text{clk},r}(0)$  were initialized as  $\mathbf{x}_{\text{clk},r}(0) \sim \mathcal{N}[\mathbf{0}_{2 \times 1}, \mathbf{P}_{\text{clk},r}]$ , where  $\mathbf{P}_{\text{clk},r} = \text{diag}[9 \times 10^4, 9 \times 10^{-2}]$  with units of  $[\text{m}^2, (\text{m/s})^2]$  corresponding to a  $1\sigma$  of  $1 \mu\text{s}$  and  $10^{-9} \text{ s/s}$  for the clock bias and drift, respectively. The values of the  $l$ -th LEO satellite clock error states  $\mathbf{x}_{\text{clk},\text{leo}_l}(0)$  were initialized as  $\mathbf{x}_{\text{clk},\text{leo}_l}(0) \sim \mathcal{N}[\mathbf{0}_{2 \times 1}, \mathbf{P}_{\text{clk},\text{leo}_l}]$ , where  $\mathbf{P}_{\text{clk},\text{leo}_l} = \text{diag}[9 \times 10^2, 9 \times 10^{-4}]$  with units of  $[\text{m}^2, (\text{m/s})^2]$  corresponding to a  $1\sigma$  of  $0.1 \mu\text{s}$  and  $10^{-10} \text{ s/s}$  for the clock bias and drift, respectively.

TABLE III  
AERIAL VEHICLE'S AND LEO SATELLITES' OSCILLATOR PARAMETERS

Quality	Coefficients $\{h_0, h_{-2}\}$
Aerial vehicle's high-quality OCXO	$\{2.6 \times 10^{-22}, 4.0 \times 10^{-26}\}$
LEO satellites' CSAC	$\{7.2 \times 10^{-21}, 2.7 \times 10^{-27}\}$

4) *Measurements*: Pseudorange rate measurements to all visible LEO satellites were generated according to (15). Pseudorange rate measurements are directly proportional to Doppler frequency observables (14) but are independent of the carrier frequency. As a result, pseudorange rate measurements were preferred over Doppler to obtain comparable measurements from different constellations which transmit downlink signals at frequencies that are orders of magnitude apart. The pseudorange rate measurement noise variances were calculated from the predicted  $C/N_0$ , which was found from the log-distance path loss model

$$(C/N_0)_l(k) = P_0 - 10 \cdot \log_{10}(d_l(k)/D_0), \quad (17)$$

where  $P_0 = 56 \text{ dB-Hz}$  is the nominal  $C/N_0$  at a distance  $D_0 = 1,000 \text{ km}$  and  $d_l(k) \triangleq \|\mathbf{r}_r(k) - \mathbf{r}_{\text{leo}_l}(k)\|$  is the distance between the receiver and the  $l$ -th LEO satellite. The pseudorange rate measurement noise variances are proportional to the square root of the inverse of  $C/N_0$ , expressed in linear units, and ranged between  $0.14$  and  $1.1 (\text{m/s})^2$ .

Pseudorange navigation observables to all visible LEO satellites were generated according to (13). The time-varying pseudorange measurement noise variances were calculated from the predicted  $C/N_0$  from (17) and ranged between  $0.43$  and  $3.52 \text{ m}^2$ , based on the distance between the aerial vehicle and the satellites.

### C. Filter Initialization

The aerial vehicle's state estimates were initialized by corrupting the aerial vehicle's true initial states with a random

sample  $\tilde{\mathbf{x}}_r(0|0)$  drawn from a zero-mean multivariate Gaussian distribution with covariance  $\mathbf{P}_{\mathbf{x}_r}(0|0)$  as follows

$$\begin{aligned} \tilde{\mathbf{x}}_r(0|0) &\sim \mathcal{N}[\mathbf{0}_{15 \times 1}, \mathbf{P}_{\mathbf{x}_r}(0|0)] \\ \mathbf{P}_{\mathbf{x}_r}(0|0) &\triangleq \text{diag}[\mathbf{P}_{\mathbf{qrr}}(0|0), \mathbf{P}_{\mathbf{b}_{\text{imu}}}(0|0)] \\ \mathbf{P}_{\mathbf{qrr}}(0|0) &= [10^{-2} \times \mathbf{I}_{3 \times 3}, 10 \times \mathbf{I}_{3 \times 3}, \mathbf{I}_{3 \times 3}] \\ \mathbf{P}_{\mathbf{b}_{\text{imu}}}(0|0) &= [10^{-3} \times \mathbf{I}_{3 \times 3}, 10^{-2} \times \mathbf{I}_{3 \times 3}], \end{aligned}$$

where  $\mathbf{P}_{\mathbf{qrr}}(0|0)$  is the initial aerial vehicle orientation, position, and velocity covariance with units of  $[\text{rad}^2, \text{m}^2, (\text{m/s})^2]$  and  $\mathbf{P}_{\mathbf{b}_{\text{imu}}}(0|0)$  is the initial IMU gyroscope and accelerometer biases covariances with units of  $[(\text{rad/s})^2, (\text{m/s}^2)^2]$ . The first three components of  $\tilde{\mathbf{x}}_r(0|0)$ , which correspond to the vector of angle errors, were used to corrupt the true initial Euler angles of the aerial vehicle. The corrupted initial Euler angles were then converted to a unit quaternion to initialize the EKF's orientation states. The remaining elements of the initial aerial vehicle's state estimates were corrupted by adding the corresponding initial error terms to the true initial states.

The  $l$ -th LEO satellite's position and velocity state estimates  $\hat{\mathbf{x}}_{\mathbf{rr}\dot{\mathbf{r}}_{\text{leo}_l}}(0|0)$  were initialized in the ECI frame, denoted by  $\{i\}$ , as follows

$$\begin{aligned} \hat{\mathbf{x}}_{\mathbf{rr}\dot{\mathbf{r}}_{\text{leo}_l}}(0|0) &\sim \mathcal{N}[\mathbf{x}_{\mathbf{rr}\dot{\mathbf{r}}_{\text{leo}_l}}(0|0), \mathbf{P}_{\mathbf{x}_{\mathbf{rr}\dot{\mathbf{r}}_{\text{leo}_l}}}(0|0)] \\ \mathbf{P}_{\mathbf{x}_{\mathbf{rr}\dot{\mathbf{r}}_{\text{leo}_l}}}(0|0) &\triangleq \text{diag}[\mathbf{P}_{\mathbf{x}_{\mathbf{r}_{\text{leo}_l}}}(0|0), \mathbf{P}_{\mathbf{x}_{\dot{\mathbf{r}}_{\text{leo}_l}}}(0|0)] \\ \mathbf{P}_{\mathbf{x}_{\mathbf{r}_{\text{leo}_l}}}(0|0) &= \mathbf{R}_{\mathbf{b}_{\text{leo}_l}}^i(0) \mathbf{P}_{\mathbf{x}_{\mathbf{r}_{\text{leo}_l}}}^{\mathbf{b}_{\text{leo}_l}}(0|0) [\mathbf{R}_{\mathbf{b}_{\text{leo}_l}}^i(0)]^T \\ \mathbf{P}_{\mathbf{x}_{\dot{\mathbf{r}}_{\text{leo}_l}}}(0|0) &= \mathbf{R}_{\mathbf{b}_{\text{leo}_l}}^i(0) \mathbf{P}_{\mathbf{x}_{\dot{\mathbf{r}}_{\text{leo}_l}}}^{\mathbf{b}_{\text{leo}_l}}(0|0) [\mathbf{R}_{\mathbf{b}_{\text{leo}_l}}^i(0)]^T, \end{aligned}$$

where  $\mathbf{x}_{\mathbf{rr}\dot{\mathbf{r}}_{\text{leo}_l}}(0|0)$  is the  $l$ -th LEO satellite's true position and velocity states in ECI and  $\mathbf{P}_{\mathbf{x}_{\mathbf{rr}\dot{\mathbf{r}}_{\text{leo}_l}}}(0|0)$  is the associated initial covariance;  $\mathbf{P}_{\mathbf{x}_{\mathbf{r}_{\text{leo}_l}}}^{\mathbf{b}_{\text{leo}_l}}(0|0) \triangleq \text{diag}[10^6, 10^1, 10^4] \text{ m}^2$  and  $\mathbf{P}_{\mathbf{x}_{\dot{\mathbf{r}}_{\text{leo}_l}}}^{\mathbf{b}_{\text{leo}_l}}(0|0) \triangleq \text{diag}[10^{-2}, 10^{-4}, 10^{-1}] (\text{m/s})^2$  are the initial LEO satellite's position and velocity covariances in the satellite's body frame  $\{\mathbf{b}_{\text{leo}_l}\}$ ; and  $\mathbf{R}_{\mathbf{b}_{\text{leo}_l}}^i(0)$  is the initial rotation matrix from the  $l$ -th LEO satellite's body frame  $\{\mathbf{b}_{\text{leo}_l}\}$  to the ECI frame  $\{i\}$ . The first entry of the LEO satellite's position and velocity covariances in the satellite's body frame corresponds to the satellites' along-track axis, the second entry is associated with the cross-track direction, and the last entry is for the radial axis. These values were carefully selected to closely match the uncertainties inherent to TLE files with the most uncertainty being in the along-track position and radial velocity, while the cross-track direction TLE errors are the least substantial as the satellites' motion is constrained in the orbital (along-track – radial) plane. The LEO satellites' process noise covariance found in [55] using a Monte Carlo analysis was used in the EKF to account for the effect of unmodeled uncertainties in the LEO satellites' orbital motion. This process noise covariance was expressed in the satellites' body frame to leverage its invariance in this frame and promote generalization. Subsequently, this process noise covariance was rotated to the ECI frame at each EKF prediction step for all LEO satellites.

The filter clock error states consisted of the difference between the receiver and each LEO satellite's clock error

states. The filter's clock bias state estimates were initialized by subtracting the estimated range from the pseudorange or carrier phase measurements while the filter's clock drift state estimates were initialized to 0.

An EKF was implemented to perform STAN and aid the INS of the aerial vehicle with navigation observables extracted from Starlink, Orbcomm, and Iridium NEXT LEO satellites' signals. Both Doppler (i.e., pseudorange rate) and pseudorange measurements were considered with an update rate of 1 Hz. Loosely-coupled GNSS updates were also performed at 1 Hz before GNSS cutoff by corrupting the aerial vehicle's true 3-D ENU position with measurement noise with covariance  $\mathbf{R}_{\text{gnss}} = \text{diag}[3, 3, 9] \text{ m}^2$ . After the first 60 seconds, GNSS updates were stopped as GNSS signals became unavailable. Altimeter updates at 1 Hz were performed throughout the flight by corrupting the aerial vehicle's true altitude with measurement noise with variance  $\sigma_{\text{alt}}^2 = 3 \text{ m}^2$ . The elevation mask was set to  $20^\circ$  and LEO satellites visible for at least 200 seconds of the 300-second trajectory were considered. This visibility duration threshold was set so that the aerial vehicle neglects LEO satellites available for a short time period. The minimum number of LEO satellites visible simultaneously to the aerial vehicle was 51 and the maximum number reached 77 visible satellites (74 Starlink, 1 Orbcomm, and 2 Iridium NEXT satellites) for 108 seconds. The satellites' trajectory are shown in Fig. 3.

#### D. Discussion

Fig. 4 shows the aerial vehicle's true trajectory, estimated GNSS-INS trajectory, and STAN trajectories computed with Doppler and pseudorange measurements. Figs. 5-6 and 9-10 show the EKF estimation error plots and associated  $\pm 3\sigma$  bounds for Starlink satellites 66 and 36, which were tracked when above the  $20^\circ$  elevation mask (i.e., within the satellite viability period) using Doppler and pseudorange measurements opportunistically extracted by the LEO receiver onboard the aerial vehicle, respectively. Moreover, Fig. 3(b) and 3(c) depict the 95% uncertainty ellipsoid of Starlink satellites 15 and 73, which were tracked using Doppler and pseudorange measurements, respectively, as well as the true and estimated satellite trajectories. Finally, the GNSS-INS and STAN EKF plots for the aerial vehicle states are shown in Fig. 8 for STAN using Doppler frequency measurements and Fig. 12 for STAN using pseudorange measurements. Table IV summarizes the navigation performance of the different frameworks.

TABLE IV  
SIMULATION RESULTS: COMPARISON OF DIFFERENT NAVIGATION FRAMEWORKS

	GNSS-INS	STAN (Doppler)	STAN (pseudorange)
Position RMSE (m)	897.4	10.6	7.3
Final Error (m)	1,536.1	37.1	15.2
Maximum Error (m)	1,536.1	37.1	15.2

The following conclusions can be drawn from these results. First, as expected, upon GNSS cut off, the GNSS-INS errors quickly diverge. In contrast, the STAN East and North EKF errors of the aerial vehicle's position slowly diverge, while

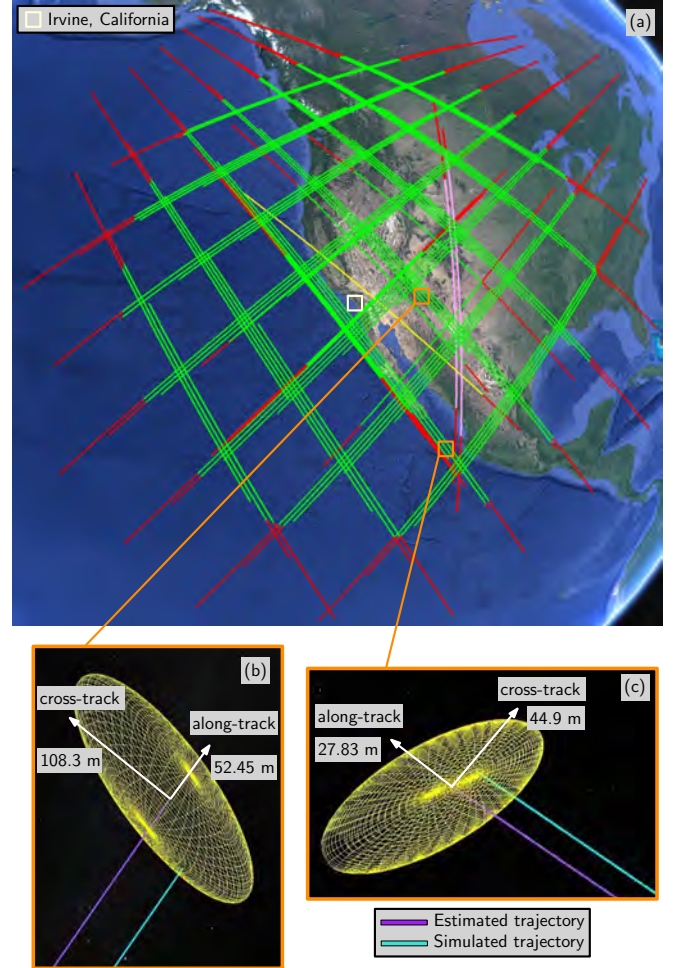


Fig. 3. (a) Simulated trajectories of 74 Starlink, 1 Orbcomm, and 2 Iridium NEXT LEO satellites. The trajectories are colored in red when the LEO satellites are below the  $20^\circ$  elevation mask. Starlink, Orbcomm, and Iridium NEXT trajectories are respectively colored in green, yellow, and pink when the satellites are visible to the aerial vehicle. (b) Estimated and true trajectories for Starlink satellite 15 tracked using Doppler measurements along with 95% uncertainty ellipsoid. (c) Estimated and true trajectories for Starlink satellite 73 tracked using pseudorange measurements along with 95% uncertainty ellipsoid. Map data: Google Earth.

the altimeter updates seem to prevent the Up EKF error from diverging. Similarly, the STAN East and North EKF errors of the aerial vehicle's velocity also diverge when GNSS is cut off, but at a much slower rate than their position counterparts. This divergence could be attributed to stochastic observability issues. The rate of divergence is a function of number of LEO satellites, vehicle's IMU grade, and receiver and LEO satellite transmitter clock qualities [73]. Note that the divergence rate of these errors is slower in the case of STAN using pseudorange measurements compared to STAN using Doppler measurements. This is consistent with the findings in [55].

Second, the orientation and IMU bias estimation errors with STAN appear to be bounded.

Third, the LEO satellites' position and velocity estimation errors are bounded and consistent during STAN with both Doppler and pseudorange measurements. Moreover, most of the initial satellite errors are corrected in the first few seconds

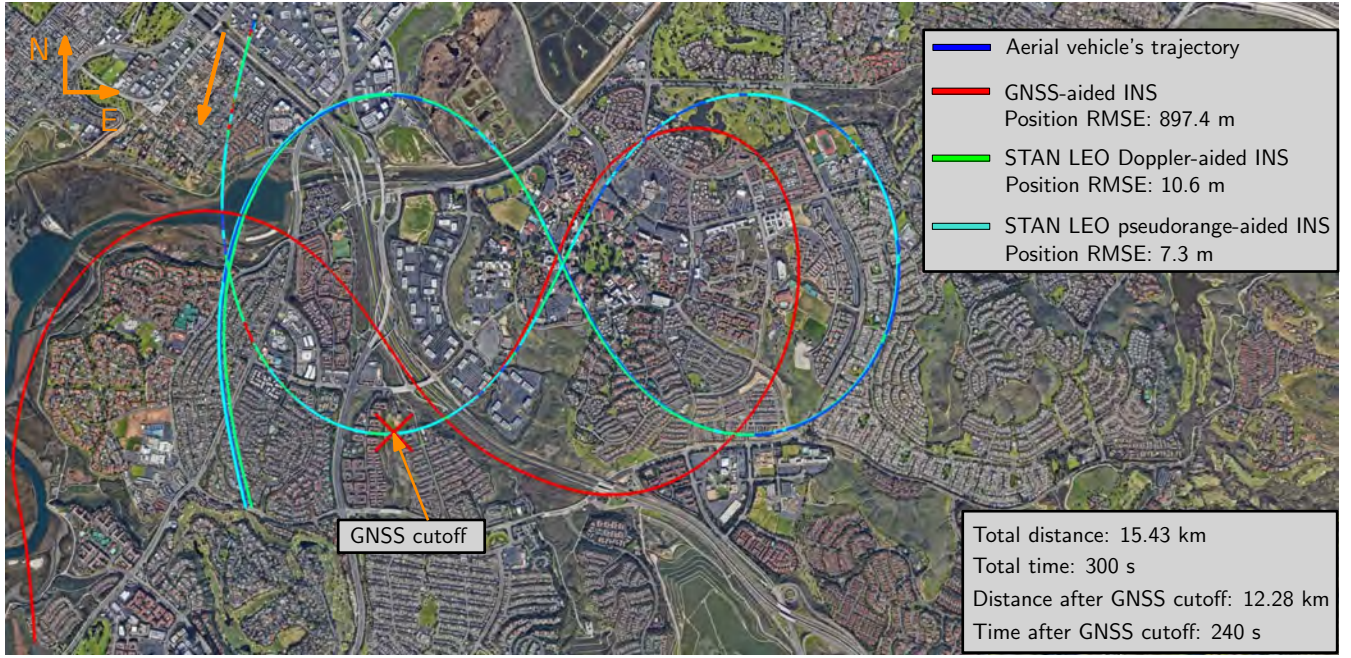


Fig. 4. Simulation results showing the aerial vehicle's trajectory and estimated trajectory with GNSS-aided INS and STAN with LEO Doppler-aided INS and LEO pseudorange-aided INS. The minimum number of LEO satellites visible simultaneously to the aerial vehicle was 51 and the maximum number reached 77 visible satellites (74 Starlink, 1 Orbcomm, and 2 Iridium NEXT satellites). Map data: Google Earth.

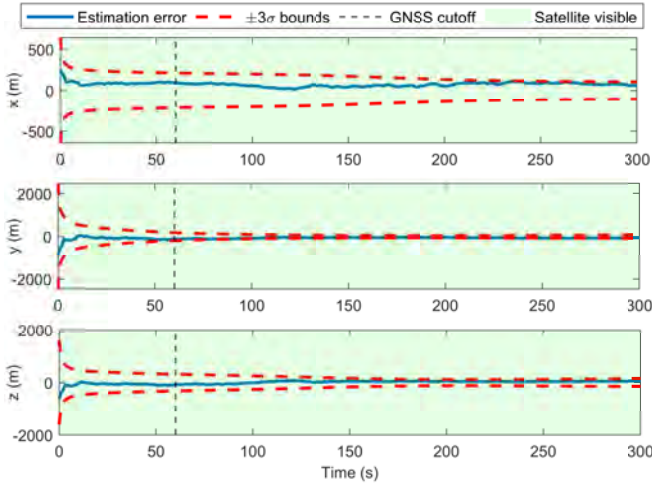


Fig. 5. Position EKF plots in the ECEF reference frame for Starlink satellite 66, tracked using Doppler measurements.

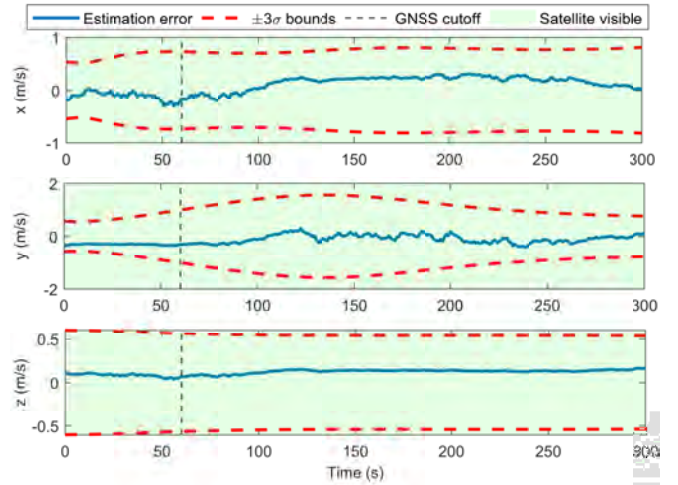


Fig. 6. Velocity EKF plots in the ECEF reference frame for Starlink satellite 66, tracked using Doppler measurements.

during the STAN tracking mode when GNSS measurements are available. It was noticed that LEO satellites with visibility period starting before GNSS cutoff are tracked more efficiently than satellites becoming visible after GNSS cutoff as the tracking receiver has a more certain estimate of its own states when GNSS is available. This observation highlights the importance of the tracking phase in satellite ephemeris refinement to enable LEO-based opportunistic navigation with the STAN framework.

Fourth, the ellipsoids in Figs. 3(b)-(c) are elongated mostly in the cross-track direction at the end of the simulation run despite having the initial uncertainty mainly in the along-track direction. This can be attributed to the fact that the cross-track direction is poorly estimable, leading to larger error and

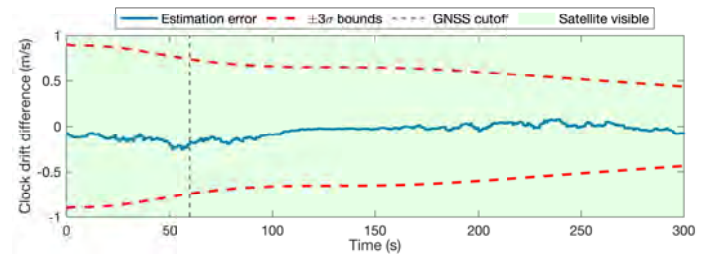


Fig. 7. Differenced clock drift EKF plot for Starlink satellite 66, tracked using Doppler measurements.

uncertainty along this axis, while the along-track error gets quickly corrected during tracking, as this direction is more estimable.

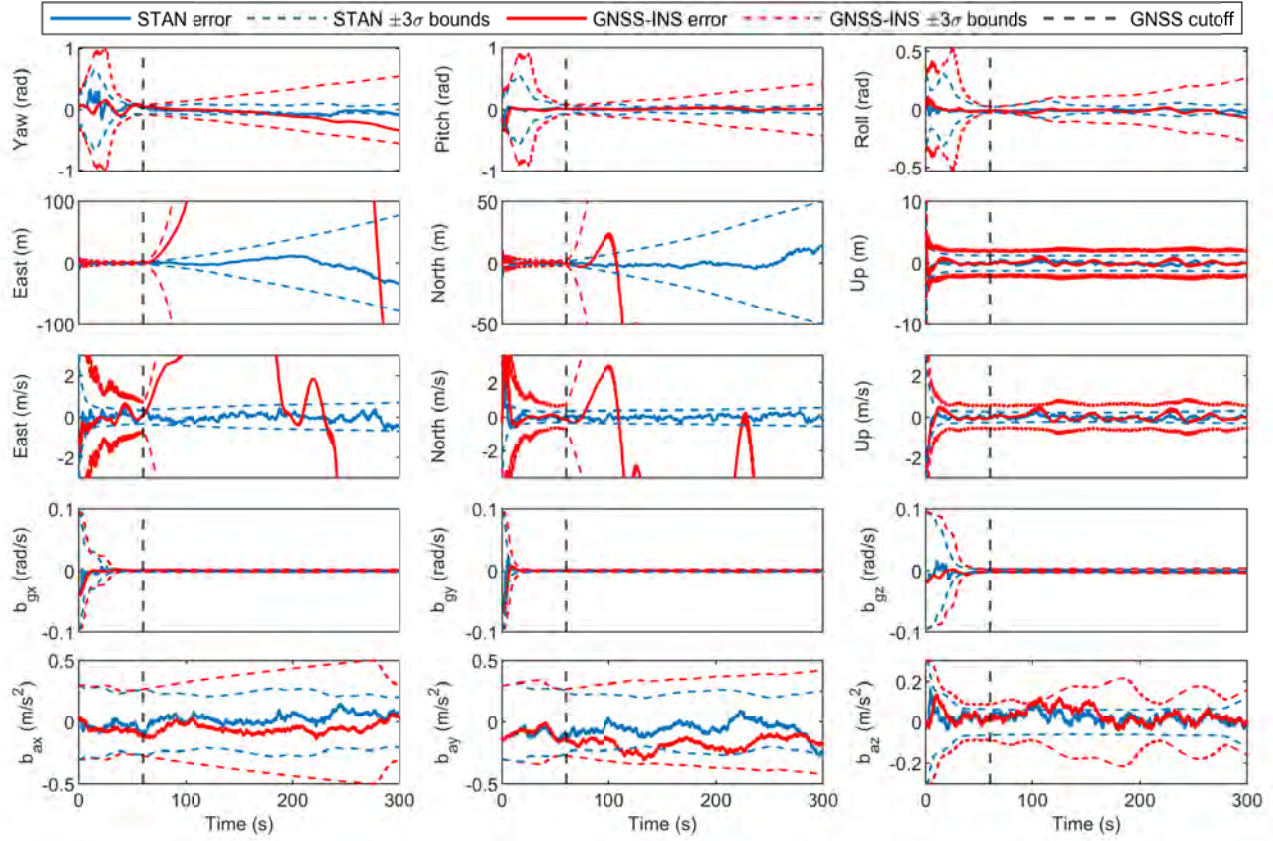


Fig. 8. EKF plots of aerial vehicle states for GNSS-INS and STAN LEO Doppler-aided INS. The first row corresponds to the orientation states of the aerial vehicle's body frame with respect to the ENU frame represented using Euler angles. The second and third rows correspond to the position and velocity states of the aerial vehicle in the ENU frame, respectively. The fourth and fifth rows correspond to the IMU's gyroscope and accelerometer biases in the aerial vehicle's body frame, respectively.

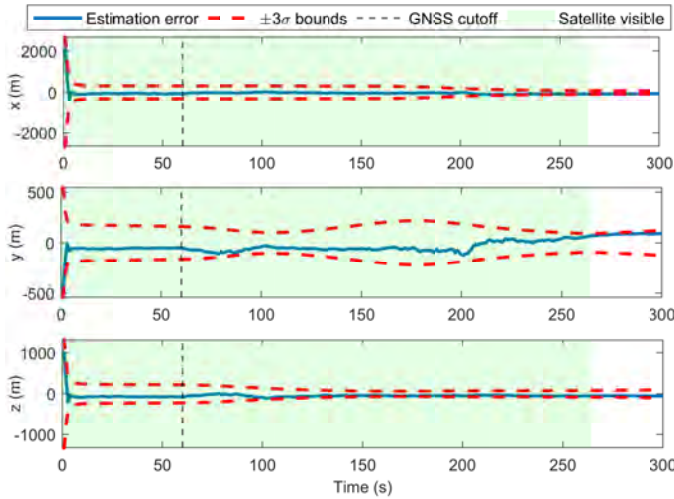


Fig. 9. Position EKF plots in the ECEF reference frame for Starlink satellite 36, tracked using pseudorange measurements.

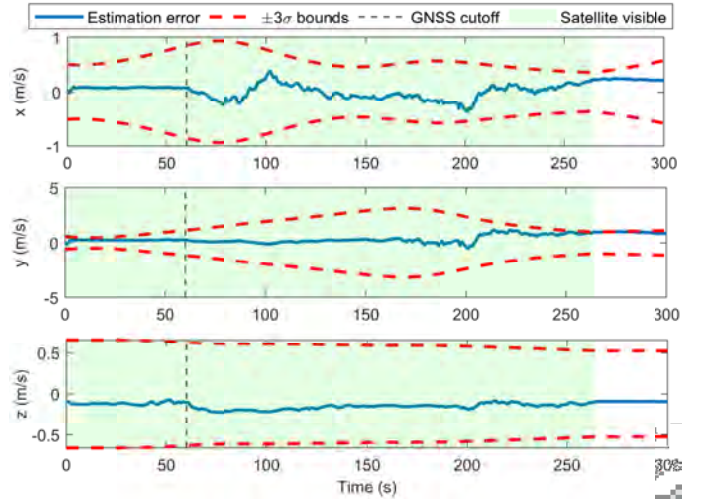


Fig. 10. Velocity EKF plots in the ECEF reference frame for Starlink satellite 36, tracked using pseudorange measurements.

Fifth, Figs. 7 and 11 show the estimation errors EKF plots of the clock drift difference between the receiver and Starlink satellite 66, tracked using Doppler measurements and the differenced clock error states (bias and drift) between the receiver and Starlink satellite 36, tracked using pseudorange

measurements, respectively, along with the associated  $\pm 3\sigma$  bounds. During tracking (i.e., satellite visibility period), it can be seen that the differenced clock error states' estimates are consistent (i.e., within the  $\pm 3\sigma$  bounds). Additionally, it is worth noting that the clock bias difference term between

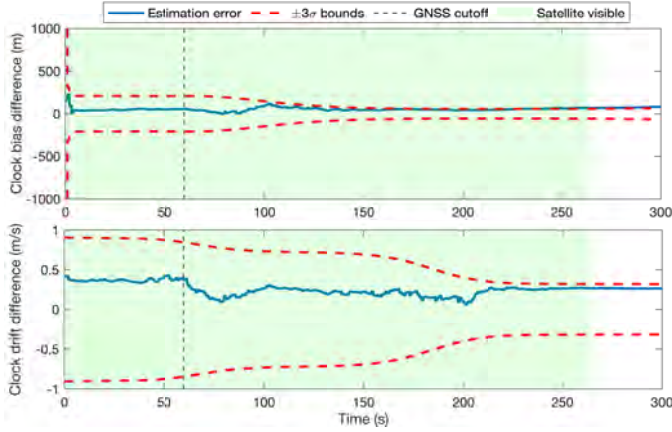


Fig. 11. Differenced clock states EKF plots for Starlink satellite 36, tracked using pseudorange measurements.

the receiver and LEO satellite transmitters is unobservable with Doppler measurements and is consequently not estimated when performing STAN with this type of observables.

Sixth, Table V summarizes the positioning results of STAN with different combinations of LEO constellations. It can be seen that no significant difference is observed between the performance of STAN with 3 LEO constellations comprising 77 satellites and that with the standalone Starlink megaconstellation (74 satellites used). As expected, the positioning errors increase as the number of LEO satellites used while performing STAN decreases. Moreover, the performance of STAN using 1 LEO satellite (Orbcomm constellation only) yields positioning errors on the same order of magnitude as a drifting GNSS-INS system (see Tables IV and V). In fact, the errors of STAN with 1 LEO satellite were a bit larger than the unaided GNSS-INS, which indicates faster filter divergence due to unobservability conditions. However, with 2 LEO satellites (Iridium NEXT constellation only) and 3 LEO satellites (Orbcomm and Iridium NEXT constellations), the STAN performance significantly improves, suggesting that at least 2 LEO satellites are needed to outperform a drifting GNSS-INS system.

Seventh, while the dilution of precision (DOP) concept is applicable to point solution estimation (i.e., batch least squares), it can be adapted to sequential filtering to quantify the effect of LEO satellite geometry. For the purpose of DOP analysis, it is assumed that only the receiver's 3-D position and clock bias are estimated in the case of STAN with pseudorange measurements and that only the receiver's 3-D position, 3-D velocity, and clock drift are estimated in the case of STAN with Doppler measurements. These assumptions are required to ensure that the number of measurements is greater than the number of estimated states, yielding an overdetermined system for which DOP calculations can be performed. The rescaling scheme from [14] was used to obtain the nondimensional DOP matrix for Doppler measurements. Moreover, a direct comparison between the pseudorange and Doppler DOP values is not fair as the three additional states estimated with Doppler measurements further contributes to the dilution of precision. Table VI shows the minimum and maximum values of geometric DOP (GDOP), horizontal DOP (HDOP), and vertical

DOP (VDOP) for pseudorange and Doppler measurements. It is interesting to note that in the pseudorange DOP calculations, the VDOP is higher than the HDOP while for the Doppler DOP values, the VDOP is lower than the HDOP. This can be attributed to the measurement type since Doppler observables give more information in the vertical direction while pseudorange measurements give less information in this direction as the LEO satellites travel overhead the receiver. The VDOP values using pseudorange measurements can be effectively lowered by the addition of terrestrial SOPs to increase the diversity in the vertical direction, as demonstrated in [92]. Finally, note that the DOP values attain their minimums around the middle of the aerial vehicle's trajectory, where the number of visible LEO satellites is the greatest.

Eighth, previous work showed that in radio simultaneous localization and mapping (radi SLAM) with stationary terrestrial SOPs, prescribed receiver motion planning strategies could significantly improve the convergence accuracy [93] and in some circumstances, they could be necessary to avoid filter divergence [94]. In STAN with megaconstellation LEO satellites, the speed and trajectory of the vehicle play less of a role in the filter convergence. This is due to the fact that the relative geometry between the receiver and the LEO satellites, represented by the unit line-of-sight (LOS) vector, is not significantly affected with changes in receiver trajectory. For reasonable vehicle-mounted receiver speeds (e.g., the aircraft considered in the simulations (Section IV) and ground vehicle considered in the experiments (Section V), the relative geometry is dictated by the LEO satellites that travel at around 7 km/s. To demonstrate the effect of changing the vehicle's trajectory on navigation performance, another trajectory was simulated in which the aerial vehicle traversed 16.34 km, the last 13.33 km of which was without GNSS. Two aerial vehicles were considered: (i) a slow vehicle, which traversed the trajectory in 300 seconds, the last 240 seconds of which without GNSS, at an average speed of 54.46 m/s; and (ii) a fast vehicle, which traversed the trajectory in 100 seconds, the last 80 seconds of which without GNSS, at an average speed of 163.38 m/s. It was observed that the position RMSE, final error, and maximum error for the slow vehicle were 11.45 m, 39.46 m, and 39.46 m, respectively; while for the fast vehicle, the values were 25.14 m, 13.55 m, and 54.33 m, respectively. Future work could consider performing a comprehensive Monte Carlo analysis to assess the effect of varying the vehicle's speed and trajectory (including motion planning strategies) on the positioning and timing performance in STAN.

## V. EXPERIMENTAL RESULTS

This section presents the first multi-constellation LEO navigation experimental results of their kind with Orbcomm, Iridium NEXT, and Starlink LEO satellites, to demonstrate the efficacy of STAN.

A ground vehicle was equipped with a VectorNav VN-100 microelectro-mechanical systems (MEMS) tactical-grade IMU, two low-noise block (LNB) downconverters to receive Starlink signals at 11.325 GHz from two different angles, a

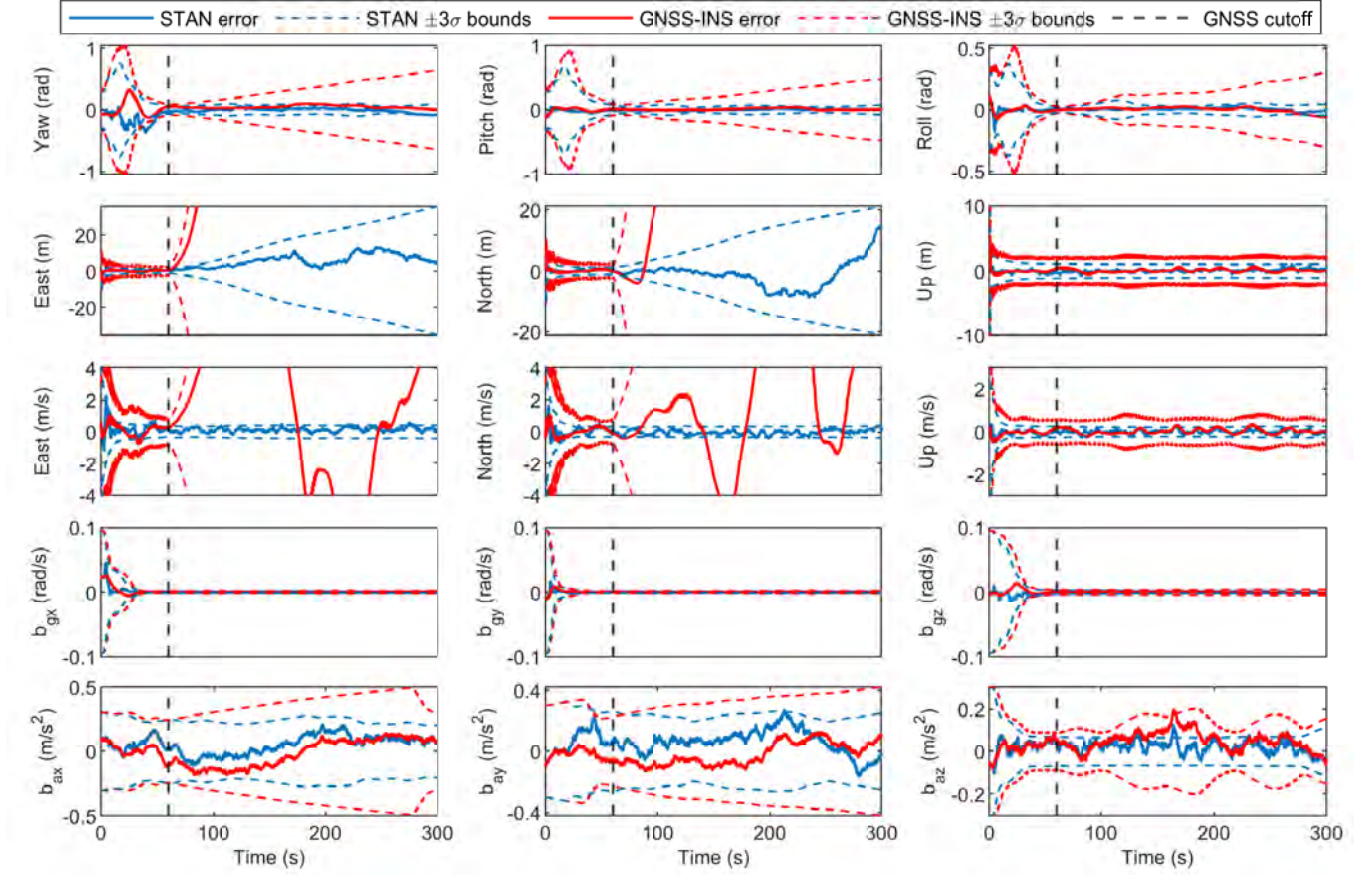


Fig. 12. EKF plots of aerial vehicle states for GNSS-INS and STAN LEO pseudorange-aided INS. The first row corresponds to the orientation states of the aerial vehicle's body frame with respect to the ENU frame represented using Euler angles. The second and third rows correspond to the position and velocity states of the aerial vehicle in the ENU frame, respectively. The fourth and fifth rows correspond to the IMU's gyroscope and accelerometer biases in the aerial vehicle's body frame, respectively.

TABLE V  
SIMULATION RESULTS: COMPARISON OF STAN USING DIFFERENT COMBINATIONS OF LEO CONSTELLATIONS

		Doppler	Pseudorange
Pos. RMSE (m)	Starlink + Orbcomm + Iridium NEXT	10.6	7.3
	Starlink	12.0	15.6
	Orbcomm + Iridium NEXT	70.6	45.2
	Iridium NEXT	136.7	94.9
	Orbcomm	1,142.1	527.9
Final Error (m)	Starlink + Orbcomm + Iridium NEXT	37.1	15.2
	Starlink	34.4	19.2
	Orbcomm + Iridium NEXT	108.4	99.6
	Iridium NEXT	125.7	457.8
	Orbcomm	2,694.9	961.6

very-high frequency (VHF) antenna to receive to Orbcomm signals at 137 MHz, and an AT1621-12 Iridium antenna to receive Iridium NEXT signals at 1626.2708 MHz. The received Starlink signals were sampled at 2.5 mega samples per seconds (Msps) with a National Instrument (NI) 2974 Universal Software Radio Peripheral (USRP), while Orbcomm and Iridium NEXT signals were sampled at 2.4 Msps with two Ettus E312 USRPs. It is worth noting that the USRPs' oscillators were synchronized and driven by an external, freely-

TABLE VI  
MINIMUM AND MAXIMUM GDOP, HDOP, AND VDOP

	Doppler	Pseudorange
Minimum GDOP	1.529	0.862
Maximum GDOP	2.230	1.061
Minimum HDOP	0.906	0.306
Maximum HDOP	1.455	0.414
Minimum VDOP	0.626	0.679
Maximum VDOP	0.956	0.811

running CDA-2990 OctoClock. The vehicle was also equipped with a Septentrio AsteRx-I V integrated GNSS-INS system, from which the ground truth was derived. The experimental setup is shown in Fig. 13.

The vehicle was driven on the CA-55 freeway next to Irvine, California, USA, for 4.15 km in 150 seconds. During the experiment, signals from 3 Starlink, 2 Orbcomm, and 1 Iridium NEXT satellites were recorded. The LEO satellites' trajectory during the experiment are shown in Fig. 14. Carrier phase navigation observables were extracted from Orbcomm satellites' signals [7] and Doppler measurements were extracted from Starlink [82] and Iridium NEXT satellites' [71] signals by an opportunistic receiver onboard the navigating

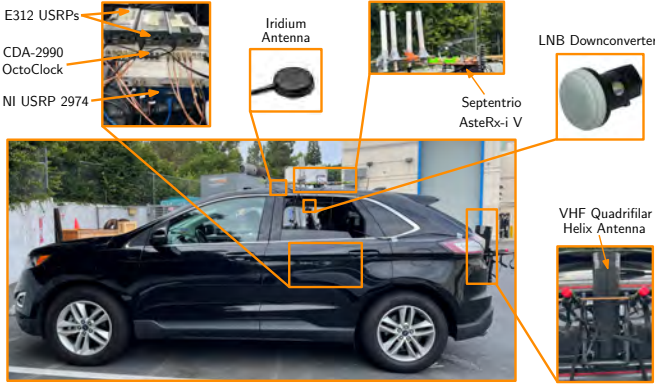


Fig. 13. Hardware setup for the ground vehicle experiment.

vehicle. Since Iridium employs a time-division multiple-access (TDMA) scheme with a frame duration of 90 ms, one can measure the Doppler shift of the signal at discrete instances, separated by the frame duration. To stitch these discontinuous Doppler measurements, the observables were interpolated at a rate that matched the measurement rate of the navigation framework.

GNSS signals were available for the first 80 seconds of the experiment but were fictitiously cut off for the last 70 seconds, during which the vehicle traveled 1.82 km. The GNSS-INS navigation solution drifted to a final heading error of  $42.36^\circ$  and a final 3-D position error of 472.69 m with a heading RMSE of  $10.43^\circ$  and a 3-D position RMSE of 118.47 m over the true trajectory. The STAN LEO-aided INS yielded a final heading error of  $5.33^\circ$  and a final 3-D position error of 27.13 m with a heading RMSE of  $4.62^\circ$  and a 3-D position RMSE of 18.43 m. These navigation results are shown in Fig. 17 and summarized in Table VII.

Figs. 15-16 show the estimates of the clock drift difference between the receiver and Iridium NEXT LEO satellite transmitters and the differenced clock error states (bias with the lumped carrier phase ambiguity from (16) and drift) between the receiver and the Orbcomm FM112 satellite, respectively, along with the associated  $\pm 3\sigma$  bounds. Unfortunately, the state estimate errors are not computable since the true differenced clock error states are not known. However, the decreasing magnitude of the  $\pm 3\sigma$  bounds reveal the convergence of the estimates. It is interesting to note how the clock error states estimates get updated and the associated  $\sigma$ -bounds decrease as soon as measurements become available at the beginning of the tracking period in Fig. 16. Finally, the empirical differenced clock drift rates were calculated by computing the drift of the carrier phase residuals (i.e., predicted ranges subtracted from the carrier phase measurements) for the Orbcomm satellites and the Doppler residuals (i.e., predicted Dopplers subtracted from the Doppler measurements) for the Iridium NEXT and Starlink satellites. These empirical differenced drift values range between  $2.2 \times 10^{-10}$  s/s for the Starlink 46048 LEO satellite and  $8.1 \times 10^{-8}$  s/s for Orbcomm FM112 satellite (equivalent to 24.2 m/s as seen in drift state plot in Fig. 16), which are characteristic of medium- to high-quality OCXOs.

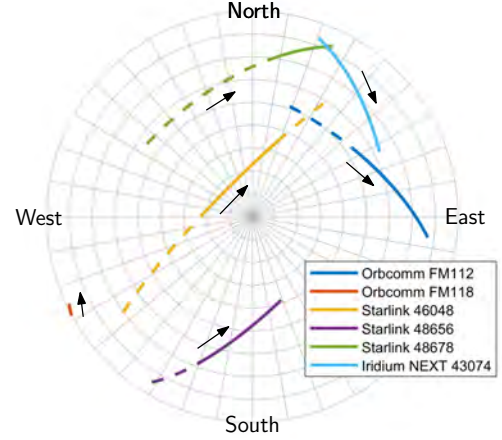


Fig. 14. Skyplot of the 3 Starlink, 2 Orbcomm, and 1 Iridium NEXT trajectories during the 150-second ground vehicle experiment (dashed) and portion of the trajectories during which the receiver opportunistically extracted navigation observables from the LEO satellites' signals (solid).

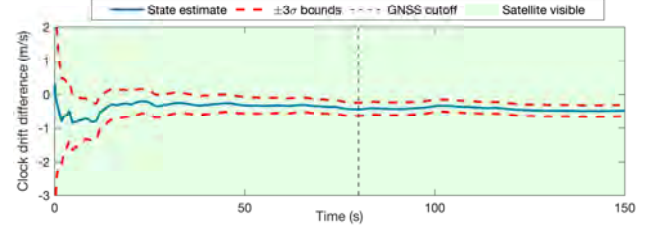


Fig. 15. Clock drift difference EKF plot for Iridium NEXT LEO satellite.

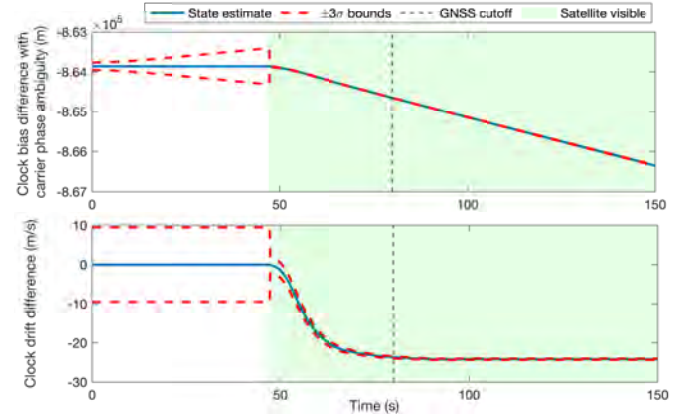


Fig. 16. Clock bias difference with lumped carrier phase ambiguity (top) and differenced clock drift (bottom) EKF plots for Orbcomm FM112 LEO satellite.

## VI. CONCLUSION

This paper presented STAN, a novel navigation framework to exploit megaconstellation LEO satellite signals for navigation. STAN estimates the navigating vehicle's states *simultaneously* with the states of LEO satellites. STAN employs a receiver that produces navigation observables from downlink LEO satellite signals. These observables are fused through an EKF to aid the vehicle's INS in a tightly coupled fashion. Simulation results were presented to demonstrate the efficacy of STAN, in which an aerial vehicle navigated for 15.43 km

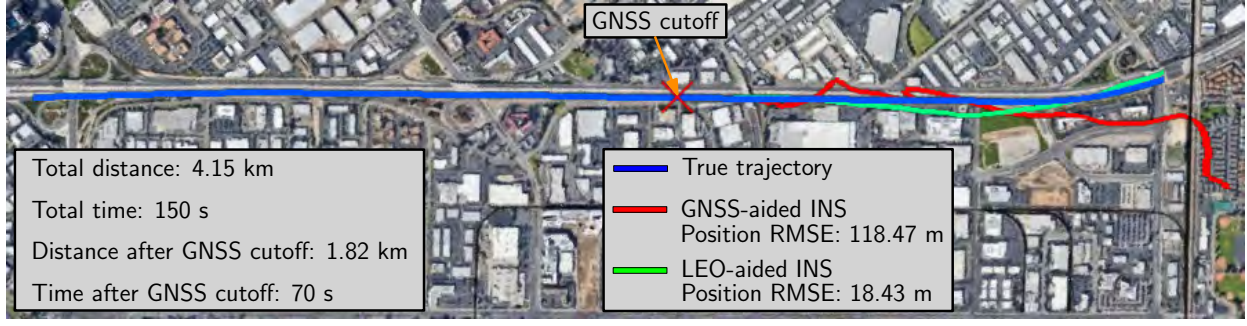


Fig. 17. Experimental results showing the ground vehicle's trajectory and estimated trajectory with GNSS-aided INS and STAN with LEO-aided INS using signals from 3 Starlink, 2 Orbcomm, and 1 Iridium NEXT satellites. Map data: Google Earth.

TABLE VII  
EXPERIMENTAL RESULTS: COMPARISON OF DIFFERENT NAVIGATION FRAMEWORKS

	GNSS-aided INS	STAN: LEO-aided INS
Position RMSE (m)	118.5	18.4
Final Position Error (m)	472.7	27.1
Maximum Position Error (m)	472.7	57.8
Heading RMSE (°)	10.4	4.6
Final Heading Error (°)	42.4	5.3
Maximum Heading Error (°)	42.4	17.7

in 300 seconds, the last 240 seconds of which were without GNSS signals. The final position error and position RMSE of a tightly-coupled GNSS-aided INS grew to 1,536 m and 897 m, respectively. In contrast, the STAN framework with 77 LEO satellites (resembling Orbcomm, Iridium NEXT, and Starlink constellations) achieved a final position error and position RMSE of 15.2 m and 7.3 m, respectively, with pseudorange measurements; and 37.1 m and 10.6 m, respectively, with Doppler measurements. The first multi-constellation LEO navigation experimental results of their kind were presented of a ground vehicle traversing 4.15 km in 150 seconds, in which GNSS signals were only available for the first 80 seconds. While the final position error and position RMSE of the vehicle's GNSS-aided INS with a tactical-grade IMU grew to 472.7 and 118.5 m, respectively; the final position error and position RMSE of STAN with received signals from 2 Orbcomm, 1 Iridium NEXT, and 3 Starlink LEO satellites were 27.1 m and 18.4 m, respectively.

## APPENDIX A EKF PREDICTION OF $\mathbf{x}_r$

The time update of  $\mathbf{x}_r$  is performed using strapdown mechanization equations in the ECI frame.

### A. Orientation Time Update

The orientation time update is given by

$${}^{b_k+1}\hat{\mathbf{q}}(k+1|j) = {}^{b_k+1}\hat{\mathbf{q}} * {}^{b_k}\hat{\mathbf{q}}(k|j), \quad (18)$$

where  ${}^{b_k+1}\hat{\mathbf{q}}$  represents an estimate of the rotation quaternion between the IMU's body frame at time  $k$  and  $k+1$  and \*

denotes the quaternion product. The quaternion  ${}^{b_k+1}\hat{\mathbf{q}}$  is computed by integrating gyroscope rotation rate data  $\boldsymbol{\omega}_{\text{imu}}(k)$  and  $\boldsymbol{\omega}_{\text{imu}}(k+1)$  using a fourth-order Runge-Kutta according to

$${}^{b_k+1}\hat{\mathbf{q}} = \bar{\mathbf{q}}_0 + \frac{T}{6} (d_1 + 2d_2 + 2d_3 + d_4),$$

where

$$d_1 = \frac{1}{2}\boldsymbol{\Omega} [{}^b\hat{\boldsymbol{\omega}}(k)] \cdot \bar{\mathbf{q}}_0, \quad d_2 = \frac{1}{2}\boldsymbol{\Omega} [\bar{\boldsymbol{\omega}}] \cdot \left( \bar{\mathbf{q}}_0 + \frac{1}{2}Td_1 \right),$$

$$d_3 = \frac{1}{2}\boldsymbol{\Omega} [\bar{\boldsymbol{\omega}}] \cdot \left( \bar{\mathbf{q}}_0 + \frac{1}{2}Td_2 \right),$$

$$d_4 = \frac{1}{2}\boldsymbol{\Omega} [{}^b\hat{\boldsymbol{\omega}}(k+1)] \cdot (\bar{\mathbf{q}}_0 + Td_3), \quad \bar{\mathbf{q}}_0 \triangleq [0, 0, 0, 1]^T,$$

$$\bar{\boldsymbol{\omega}} \triangleq \frac{1}{2} [{}^b\hat{\boldsymbol{\omega}}(k) + {}^b\hat{\boldsymbol{\omega}}(k+1)],$$

where  $\boldsymbol{\Omega}[\cdot] \in \mathbb{R}^{4 \times 4}$  is given by

$$\boldsymbol{\Omega}[\mathbf{a}] \triangleq \begin{bmatrix} -[\mathbf{a} \times] & \mathbf{a} \\ -\mathbf{a}^T & 0 \end{bmatrix}, \quad \mathbf{a} \triangleq [a_1, a_2, a_3]^T,$$

$[\mathbf{a} \times] \in \mathbb{R}^{3 \times 3}$  is the skew-symmetric matrix form of  $\mathbf{a}$  and is found by

$$[\mathbf{a} \times] \triangleq \begin{bmatrix} 0 & -a_3 & a_2 \\ a_3 & 0 & -a_1 \\ -a_2 & a_1 & 0 \end{bmatrix},$$

and  ${}^b\hat{\boldsymbol{\omega}}(k)$  is the bias-compensated rotation rate measurement, which is computed according to

$${}^b\hat{\boldsymbol{\omega}}(k) = \boldsymbol{\omega}_{\text{imu}}(k) - \hat{\mathbf{b}}_{\text{gyr}}(k|j), \quad (19)$$

### B. Velocity and Position Time Update

IMU specific force measurements are integrated using trapezoidal integration to perform a time update of the position and velocity in the ECI coordinate frame. Assuming that the variation of the gravity acceleration  ${}^i\mathbf{g}$  is negligible over the integration interval, the velocity time update is performed as

$$\begin{aligned} {}^i\hat{\mathbf{r}}_b(k+1|j) &= {}^i\hat{\mathbf{r}}_b(k|j) + \frac{T}{2} [{}^i\hat{\mathbf{a}}(k) + {}^i\hat{\mathbf{a}}(k+1)] \\ &\quad + {}^i\mathbf{g}({}^i\mathbf{r}_b(k))T, \end{aligned} \quad (20)$$

where  ${}^i\hat{\mathbf{a}}$  and  ${}^b\mathbf{a}$  are the transformed bias-compensated specific force and untransformed bias-compensated specific force, respectively, which are given by

$${}^i\hat{\mathbf{a}}(k) \triangleq \hat{\mathbf{R}}^T(k) {}^b\hat{\mathbf{a}}(k), \quad (21)$$

$${}^b\mathbf{a}(k) = \hat{\mathbf{a}}_{\text{imu}}(k) - \hat{\mathbf{b}}_{\text{acc}}(k|j), \quad (22)$$

and  $\hat{\mathbf{R}}(k) \triangleq \mathbf{R} \begin{bmatrix} \hat{\mathbf{q}}(k|j) \end{bmatrix}$  is the rotation matrix from frame  $\{i\}$  to frame  $\{b\}$  associated with the quaternion  ${}^b\hat{\mathbf{q}}(k|j)$ .

The position time update is performed according to

$${}^i\hat{\mathbf{r}}_b(k+1|j) = {}^i\hat{\mathbf{r}}_b(k|j) + \frac{T}{2} \left[ {}^i\hat{\mathbf{r}}_b(k|j) + {}^i\hat{\mathbf{r}}(k+1|j) \right].$$

## APPENDIX B

### INS STATE TRANSITION AND PROCESS NOISE COVARIANCE MATRICES

The calculation of the discrete-time linearized INS state transition matrix  $\Phi_{\text{ins}}$  and process noise covariance  $\mathbf{Q}_{\text{ins}}$  are performed using strapdown INS equations as described in [74], [89]. The discrete-time linearized INS state transition matrix  $\Phi_{\text{ins}}$  is given by

$$\Phi_{\text{ins}} = \begin{bmatrix} \mathbf{I}_{3 \times 3} & \mathbf{0}_{3 \times 3} & \mathbf{0}_{3 \times 3} & \Phi_{qb_{\text{gyr}}} & \mathbf{0}_{3 \times 3} \\ \Phi_{rq} & \mathbf{I}_{3 \times 3} & T\mathbf{I}_{3 \times 3} & \Phi_{rb_{\text{gyr}}} & \Phi_{rb_{\text{acc}}} \\ \Phi_{r\dot{q}} & \mathbf{0}_{3 \times 3} & \mathbf{I}_{3 \times 3} & \Phi_{r\dot{b}_{\text{gyr}}} & \Phi_{r\dot{b}_{\text{acc}}} \\ \mathbf{0}_{3 \times 3} & \mathbf{0}_{3 \times 3} & \mathbf{0}_{3 \times 3} & \mathbf{I}_{3 \times 3} & \mathbf{0}_{3 \times 3} \\ \mathbf{0}_{3 \times 3} & \mathbf{0}_{3 \times 3} & \mathbf{0}_{3 \times 3} & \mathbf{0}_{3 \times 3} & \mathbf{I}_{3 \times 3} \end{bmatrix},$$

where

$$\Phi_{qb_{\text{gyr}}} = -\frac{T}{2} \left[ \hat{\mathbf{R}}^T(k) + \hat{\mathbf{R}}^T(k+1) \right],$$

$$\Phi_{rq} = -\frac{T}{2} \left[ [{}^i\hat{\mathbf{a}}(k) + {}^i\hat{\mathbf{a}}(k+1)] \times \right], \quad \Phi_{r\dot{q}} = \frac{T}{2} \Phi_{rq},$$

$$\Phi_{r\dot{b}_{\text{gyr}}} = -\frac{T}{2} [{}^i\hat{\mathbf{a}}(k) \times] \Phi_{qb_{\text{gyr}}}, \quad \Phi_{r\dot{b}_{\text{acc}}} = \Phi_{qb_{\text{gyr}}},$$

$$\Phi_{rb_{\text{gyr}}} = \frac{T}{2} \Phi_{r\dot{b}_{\text{gyr}}}, \quad \Phi_{rb_{\text{acc}}} = \frac{T}{2} \Phi_{r\dot{b}_{\text{acc}}}.$$

The discrete-time linearized INS process noise covariance  $\mathbf{Q}_{\text{ins}}$  is given by

$$\mathbf{Q}_{\text{ins}} = \frac{T}{2} \left( \Phi_{\text{ins}} \mathbf{N}_c \Phi_{\text{ins}}^T + \mathbf{N}_c \right),$$

where

$$\mathbf{N}_c = \text{diag}[\mathbf{S}_{\text{ng}}, \mathbf{0}_{3 \times 3}, \mathbf{S}_{\text{na}}, \mathbf{S}_{\text{bg}}, \mathbf{S}_{\text{ba}}],$$

with  $\mathbf{S}_{\text{ng}} = T\mathbf{Q}_{\text{ng}}$  and  $\mathbf{S}_{\text{na}} = T\mathbf{Q}_{\text{na}}$  are the PSD matrices of the gyroscope's and accelerometer's random noise, respectively, and  $\mathbf{S}_{\text{bg}} = \mathbf{Q}_{\text{bg}}/T$  and  $\mathbf{S}_{\text{ba}} = \mathbf{Q}_{\text{ba}}/T$  are the PSD matrices of the gyroscope's and accelerometer's bias instability, respectively.

## APPENDIX C

### EKF STATE MEASUREMENT UPDATE EQUATIONS

The standard EKF equations are modified to deal with the 3-D orientation error correction, which contains one less dimension than the 4-D orientation quaternion estimate, as described in Subsection III-E1. To this end, the state estimate is separated into two parts according to  $\hat{\mathbf{x}} \triangleq \begin{bmatrix} {}^b\hat{\mathbf{q}}^T, \hat{\mathbf{y}}^T \end{bmatrix}^T$ , where  ${}^b\hat{\mathbf{q}} \in \mathbb{R}^4$  is the orientation quaternion estimate and  $\hat{\mathbf{y}} \in \mathbb{R}^{12+8M}$  is a vector containing the remaining estimates of  $\mathbf{x}$ . Next, the EKF correction vector  $\check{\mathbf{x}}(k+1)$ , which is to be applied to the current state prediction  $\hat{\mathbf{x}}(k+1|j)$  to produce

the EKF state measurement update  $\hat{\mathbf{x}}(k+1|k+1)$ , is computed and partitioned according to

$$\check{\mathbf{x}}(k+1) = \mathbf{K}(k+1)\boldsymbol{\nu}(k+1|j) \triangleq \begin{bmatrix} \check{\boldsymbol{\theta}}(k+1) \\ \check{\mathbf{y}}(k+1) \end{bmatrix},$$

where  $\mathbf{K}(k+1)$  is the standard Kalman gain,  $\boldsymbol{\nu}(k+1|j) \triangleq \mathbf{z}(k+1) - \hat{\mathbf{z}}(k+1|j)$  is the measurement innovations,  $\check{\boldsymbol{\theta}} \in \mathbb{R}^3$  is the orientation correction, and  $\check{\mathbf{y}} \in \mathbb{R}^{12+8M}$  is a vector containing the remaining corrections. Finally, the EKF state measurement update  $\hat{\mathbf{x}}(k+1|k+1)$  is computed by applying  $\check{\boldsymbol{\theta}}(k+1)$  to  ${}^b\hat{\mathbf{q}}(k+1|j)$  and  $\check{\mathbf{y}}(k+1)$  to  $\hat{\mathbf{y}}(k+1|j)$  as follows

$$\hat{\mathbf{x}}(k+1|k+1) = \begin{bmatrix} {}^b\hat{\mathbf{q}}(k+1|j) * \left[ \frac{1}{2}\check{\boldsymbol{\theta}}^T(k+1), \sqrt{1 - \frac{1}{4}\check{\boldsymbol{\theta}}^T(k+1)\check{\boldsymbol{\theta}}(k+1)} \right]^T \\ \hat{\mathbf{y}}(k+1|j) + \check{\mathbf{y}}(k+1) \end{bmatrix}.$$

## ACKNOWLEDGMENTS

The authors would like to thank Joe Khalife, Joshua Morales, and Mohammad Neiavaie for insightful discussions and Jamil Haidar-Ahmad for help with data collection.

## REFERENCES

- [1] G. Curzi, D. Modenini, and P. Tortora, "Large constellations of small satellites: A survey of near future challenges and missions," *Aerospace*, vol. 7, no. 9, pp. 1–18, September 2020.
- [2] S. Liu, Z. Gao, Y. Wu, D. Kwan Ng, X. Gao, K. Wong, S. Chatzinotas, and B. Ottersten, "LEO satellite constellations for 5G and beyond: How will they reshape vertical domains?" *IEEE Communications Magazine*, vol. 59, no. 7, pp. 30–36, July 2021.
- [3] R. Ioannides, T. Pany, and G. Gibbons, "Known vulnerabilities of global navigation satellite systems, status, and potential mitigation techniques," *Proceedings of the IEEE*, vol. 104, no. 6, pp. 1174–1194, February 2016.
- [4] T. Reid, A. Neish, T. Walter, and P. Enge, "Broadband LEO constellations for navigation," *NAVIGATION, Journal of the Institute of Navigation*, vol. 65, no. 2, pp. 205–220, 2018.
- [5] Z. Kassas, J. Morales, and J. Khalife, "New-age satellite-based navigation – STAN: simultaneous tracking and navigation with LEO satellite signals," *Inside GNSS Magazine*, vol. 14, no. 4, pp. 56–65, 2019.
- [6] T. Reid, K. Gunning, A. Perkins, S. Lo, and T. Walter, "Going back for the future: Large/mega LEO constellations for navigation," in *Proceedings of ION GNSS Conference*, September 2019, pp. 2452–2468.
- [7] J. Khalife, M. Neiavaie, and Z. Kassas, "Navigation with differential carrier phase measurements from megaconstellation LEO satellites," in *Proceedings of IEEE/ION Position, Location, and Navigation Symposium*, April 2020, pp. 1393–1404.
- [8] J. Fischer, "Resilient timekeeping for critical infrastructure," in *Proceedings of ION Precise Time and Time Interval Systems and Applications Meeting*, 2020, pp. 234–240.
- [9] R. Morales-Ferre, E. Lohan, G. Falco, and E. Falletti, "GDOP-based analysis of suitability of LEO constellations for future satellite-based positioning," in *Proceedings of IEEE International Conference on Wireless for Space and Extreme Environments*, 2020, pp. 147–152.
- [10] D. Racelis and M. Joerger, "Impact of cascading faults on megaconstellation-augmented GNSS PPP integrity," in *Proceedings of ION GNSS Conference*, 2020, pp. 3055–3070.
- [11] Z. Kassas, J. Khalife, M. Neiavaie, and T. Mortlock, "Opportunity comes knocking: overcoming GPS vulnerabilities with other satellites' signals," *Inside Unmanned Systems Magazine*, pp. 30–35, June/July 2020.
- [12] P. Iannucci and T. Humphreys, "Economical fused LEO GNSS," in *Proceedings of IEEE/ION Position, Location and Navigation Symposium*, 2020, pp. 426–443.
- [13] S. Thompson, S. Martin, and D. Bevely, "Single differenced Doppler positioning with low Earth orbit signals of opportunity and angle of arrival estimation," in *Proceedings of ION International Technical Meeting*, 2020, pp. 497–509.

- [14] M. Psiaki, "Navigation using carrier Doppler shift from a LEO constellation: TRANSIT on steroids," *NAVIGATION, Journal of the Institute of Navigation*, vol. 68, no. 3, pp. 621–641, September 2021.
- [15] Z. Kassas, M. Neinavaie, J. Khalife, N. Khairallah, J. Haidar-Ahmad, S. Kozhaya, and Z. Shadram, "Enter LEO on the GNSS stage: Navigation with Starlink satellites," *Inside GNSS Magazine*, vol. 16, no. 6, pp. 42–51, 2021.
- [16] M. Li, T. Xu, M. Guan, F. Gao, and N. Jiang, "LEO-constellation-augmented multi-GNSS real-time PPP for rapid re-convergence in harsh environments," *GPS Solutions*, vol. 26, no. 1, pp. 1–12, 2022.
- [17] R. Cassel, D. Scherer, D. Wilburne, J. Hirschauer, and J. Burke, "Impact of improved oscillator stability on LEO-based satellite navigation," in *Proceedings of ION International Technical Meeting*, January 2022, pp. 893–905.
- [18] M. Hartnett, "Performance assessment of navigation using carrier Doppler measurements from multiple LEO constellations," Master's thesis, Air Force Institute of Technology, Ohio, USA, 2022.
- [19] F. Prol, R. Ferre, Z. Saleem, P. Välisuo, C. Pinell, E. Lohan, M. Elsanhoury, M. Elmusrati, S. Islam, K. Celikbilek, K. Selvan, J. Yliaho, K. Rutledge, A. Ojala, L. Ferranti, J. Praks, M. Bhuiyan, S. Kaasalainen, and H. Kuusniemi, "Position, navigation, and timing (PNT) through low earth orbit (LEO) satellites: A survey on current status, challenges, and opportunities," *IEEE Access*, vol. 10, pp. 83 971–84 002, 2022.
- [20] M. Jiang, H. Qin, C. Zhao, and G. Sun, "LEO Doppler-aided GNSS position estimation," *GPS Solutions*, vol. 26, no. 1, pp. 1–18, 2022.
- [21] K. Wang and A. El-Mowafy, "LEO satellite clock analysis and prediction for positioning applications," *Geo-spatial Information Science*, vol. 25, no. 1, pp. 14–33, 2022.
- [22] T. Reid, B. Chan, A. Goel, K. Gunning, B. Manning, J. Martin, A. Neish, A. Perkins, and P. Tarantino, "Satellite navigation for the age of autonomy," in *Proceedings of IEEE/ION Position, Location and Navigation Symposium*, 2020, pp. 342–352.
- [23] A. Nardin, F. Dosis, and J. Fraire, "Empowering the tracking performance of LEO-based positioning by means of meta-signals," *IEEE Journal of Radio Frequency Identification*, vol. 5, no. 3, pp. 244–253, 2021.
- [24] J. Ji, Y. Liu, W. Chen, D. Wu, H. Lu, and J. Zhang, "A novel signal design and performance analysis in NavCom based on LEO constellation," *Sensors*, vol. 21, no. 23, pp. 8235–8262, December 2021.
- [25] S. Bilardi, "A GNSS signal simulator and processor for evaluating acquisition and tracking of GPS-like signals from satellites in LEO," Master's thesis, University of Colorado at Boulder, CO, USA, 2021.
- [26] D. Egea-Roca, J. Lopez-Salcedo, G. Seco-Granados, and E. Falletti, "Performance analysis of a multi-slope chirp spread spectrum signal for PNT in a LEO constellation," in *Proceedings of Workshop on Satellite Navigation Technology*, September 2022, pp. 1–9.
- [27] P. Iannucci and T. Humphreys, "Fused low-Earth-orbit GNSS," *IEEE Transactions on Aerospace and Electronic Systems*, 2022, accepted.
- [28] L. Gill, D. Grenier, and J. Chouinard, "Use of XM radio satellite signal as a source of opportunity for passive coherent location," *IET Radar, Sonar Navigation*, vol. 5, no. 5, pp. 536–544, June 2011.
- [29] J. Khalife and Z. Kassas, "Receiver design for Doppler positioning with LEO satellites," in *Proceedings of IEEE International Conference on Acoustics, Speech and Signal Processing*, May 2019, pp. 5506–5510.
- [30] R. Landry, A. Nguyen, H. Rasae, A. Amrhar, X. Fang, and H. Benzerrouk, "Iridium Next LEO satellites as an alternative PNT in GNSS denied environments—part 1," *Inside GNSS Magazine*, vol. 14, no. 3, pp. 56–64, May 2019.
- [31] H. Benzerrouk, Q. Nguyen, F. Xiaoxing, A. Amrhar, A. Nebylov, and R. Landry, "Alternative PNT based on Iridium Next LEO satellites Doppler/INS integrated navigation system," in *Proceedings of Saint Petersburg International Conference on Integrated Navigation Systems*, May 2019, pp. 1–10.
- [32] Q. Wei, X. Chen, and Y. Zhan, "Exploring implicit pilots for precise estimation of LEO satellite downlink Doppler frequency," *IEEE Communications Letters*, vol. 24, no. 10, pp. 2270–2274, 2020.
- [33] F. Farhangian, H. Benzerrouk, and R. Landry, "Opportunistic in-flight INS alignment using LEO satellites and a rotary IMU platform," *Aerospace*, vol. 8, no. 10, pp. 280–281, 2021.
- [34] M. Neinavaie, J. Khalife, and Z. Kassas, "Blind Doppler tracking and beacon detection for opportunistic navigation with LEO satellite signals," in *Proceedings of IEEE Aerospace Conference*, 2021, pp. 1–8.
- [35] N. Jardak and Q. Jault, "The potential of LEO satellite-based opportunistic navigation for high dynamic applications," *Sensors*, vol. 22, no. 7, pp. 2541–2565, 2022.
- [36] C. Zhao, H. Qin, and Z. Li, "Doppler measurements from multiconstellations in opportunistic navigation," *IEEE Transactions on Instrumentation and Measurement*, vol. 71, pp. 1–9, 2022.
- [37] C. Huang, H. Qin, C. Zhao, and H. Liang, "Phase - time method: Accurate Doppler measurement for Iridium NEXT signals," *IEEE Transactions on Aerospace and Electronic Systems*, vol. 58, no. 6, pp. 5954–5962, 2022.
- [38] J. Raquet *et al.*, "Position, navigation, and timing technologies in the 21st century," J. Morton, F. van Diggelen, J. Spilker, Jr., and B. Parkinson, Eds. Wiley-IEEE, 2021, vol. 2, Part D: Position, Navigation, and Timing Using Radio Signals-of-Opportunity, ch. 35–43, pp. 1115–1412, doi: 10.1002/9781119458555.ch35.
- [39] J. McElroy, "Navigation using signals of opportunity in the AM transmission band," Master's thesis, Air Force Institute of Technology, Wright-Patterson Air Force Base, Ohio, USA, 2006.
- [40] X. Chen, Q. Wei, F. Wang, Z. Jun, S. Wu, and A. Men, "Super-resolution time of arrival estimation for a symbiotic FM radio data system," *IEEE Transactions on Broadcasting*, vol. 66, no. 4, pp. 847–856, December 2020.
- [41] C. Yang, T. Nguyen, and E. Blasch, "Mobile positioning via fusion of mixed signals of opportunity," *IEEE Aerospace and Electronic Systems Magazine*, vol. 29, no. 4, pp. 34–46, April 2014.
- [42] L. Chen, O. Julien, P. Thevenon, D. Serant, A. Pena, and H. Kuusniemi, "TOA estimation for positioning with DVB-T signals in outdoor static tests," *IEEE Transactions on Broadcasting*, vol. 61, no. 4, pp. 625–638, 2015.
- [43] K. Shamaei, J. Khalife, and Z. Kassas, "Exploiting LTE signals for navigation: Theory to implementation," *IEEE Transactions on Wireless Communications*, vol. 17, no. 4, pp. 2173–2189, April 2018.
- [44] J. del Peral-Rosado, R. Raulefs, J. Lopez-Salcedo, and G. Seco-Granados, "Survey of cellular mobile radio localization methods: from 1G to 5G," *IEEE Communications Surveys & Tutorials*, vol. 20, no. 2, pp. 1124–1148, 2018.
- [45] P. Wang and Y. Morton, "Multipath estimating delay lock loop for LTE signal TOA estimation in indoor and urban environments," *IEEE Transactions on Wireless Communications*, vol. 19, no. 8, pp. 5518–5530, 2020.
- [46] J. Gante, L. Sousa, and G. Falcao, "Dethroning GPS: Low-power accurate 5G positioning systems using machine learning," *IEEE Journal on Emerging and Selected Topics in Circuits and Systems*, vol. 10, no. 2, pp. 240–252, June 2020.
- [47] K. Shamaei and Z. Kassas, "Receiver design and time of arrival estimation for opportunistic localization with 5G signals," *IEEE Transactions on Wireless Communications*, vol. 20, no. 7, pp. 4716–4731, 2021, doi: 10.1109/TWC.2021.3061985.
- [48] J. Khalife and Z. Kassas, "Precise UAV navigation with cellular carrier phase measurements," in *Proceedings of IEEE/ION Position, Location, and Navigation Symposium*, April 2018, pp. 978–989.
- [49] M. Maaref and Z. Kassas, "Autonomous integrity monitoring for vehicular navigation with cellular signals of opportunity and an IMU," *IEEE Transactions on Intelligent Transportation Systems*, vol. 23, no. 6, pp. 5586–5601, June 2022.
- [50] E. Kulu, "Satellite constellations—2021 industry survey and trends," in *Proceedings of Annual Small Satellite Conference*, September 2021, pp. 1–20.
- [51] J. Morales and Z. Kassas, "Tightly-coupled inertial navigation system with signals of opportunity aiding," *IEEE Transactions on Aerospace and Electronic Systems*, vol. 57, no. 3, pp. 1930–1948, 2021.
- [52] T. Reid, T. Walter, P. Enge, D. Lawrence, H. Cobb, G. Gutt, M. O'Connor, and D. Whelan, "Position, navigation, and timing technologies in the 21st century," J. Morton, F. van Diggelen, J. Spilker, Jr., and B. Parkinson, Eds. Wiley-IEEE, 2021, vol. 2, ch. 43: Navigation from low Earth orbit – Part 1: concept, current capability, and future promise, pp. 1359–1379.
- [53] Z. Kassas, "Position, navigation, and timing technologies in the 21st century," J. Morton, F. van Diggelen, J. Spilker, Jr., and B. Parkinson, Eds. Wiley-IEEE, 2021, vol. 2, ch. 43: Navigation from low Earth orbit – Part 2: models, implementation, and performance, pp. 1381–1412.
- [54] D. Lawrence, H. Cobb, G. Gutt, M. O'Connor, T. Reid, T. Walter, and D. Whelan, "Navigation from LEO: Current capability and future promise," *GPS World Magazine*, vol. 28, no. 7, pp. 42–48, July 2017.
- [55] N. Khairallah and Z. Kassas, "Ephemeris closed-loop tracking of LEO satellites with pseudorange and Doppler measurements," in *Proceedings of ION GNSS Conference*, September 2021, pp. 2544–2555.
- [56] R. Sabbagh and Z. Kassas, "Observability analysis of receiver localization via pseudorange measurements from a single LEO satellite," *IEEE Control Systems Letters*, vol. 7, no. 3, pp. 571–576, 2023.

- [57] K. Wang and A. El-Mowafy, "Proposed orbital products for positioning using mega-constellation LEO satellites," *Remote Sensing*, vol. 20, no. 20, pp. 5806–5826, October 2020.
- [58] S. Shuster, "A survey and performance analysis of orbit propagators for LEO, GEO, and highly elliptical orbits," Master's thesis, Utah State University, Utah, USA, 2017.
- [59] O. Montenbruck and E. Gill, *Satellite orbits: models, methods, and applications*. Springer, 2000.
- [60] B. Schutz, B. Tapley, and G. Born, *Statistical orbit determination*. Elsevier, 2004.
- [61] North American Aerospace Defense Command (NORAD), "Two-line element sets," <http://celestrak.com/NORAD/elements/>.
- [62] J. Vetter, "Fifty years of orbit determination: Development of modern astrodynamics methods," *Johns Hopkins APL Technical Digest*, vol. 27, no. 3, pp. 239–252, November 2007.
- [63] D. Vallado, "An analysis of state vector propagation using differing flight dynamics programs," in *Proceedings of the AAS Space Flight Mechanics Conference*, vol. 120, January 2005, pp. 1563–1592.
- [64] D. Hobbs and P. Bohn, "Precise orbit determination for low Earth orbit satellites," *Annals of the Marie Curie Fellowships*, vol. 4, pp. 128–135, 2006.
- [65] A. Amir, W. Kan, and A. El-Mowafy, "Precise orbit determination of LEO satellites based on undifferenced GNSS observations," *Journal of surveying engineering*, vol. 18, no. 1, pp. 1–22, 2021.
- [66] A. Hauschild and O. Montenbruck, "Precise real-time navigation of LEO satellites using GNSS broadcast ephemerides," *NAVIGATION, Journal of the Institute of Navigation*, vol. 68, no. 2, pp. 419–432, 2021.
- [67] H. Peng and X. Bai, "Comparative evaluation of three machine learning algorithms on improving orbit prediction accuracy," *Astrodynamics*, vol. 3, no. 4, pp. 325–343, 2019.
- [68] D. Shen, J. Lu, G. Chen, E. Blasch, C. Sheaff, M. Pugh, and K. Pham, "Methods of machine learning for space object pattern classification," in *Proceedings of IEEE National Aerospace and Electronics Conference*, 2019, pp. 565–572.
- [69] B. Li, J. Huang, Y. Feng, F. Wang, and J. Sang, "A machine learning-based approach for improved orbit predictions of LEO space debris with sparse tracking data from a single station," *IEEE Transactions on Aerospace and Electronic Systems*, vol. 56, no. 6, pp. 4253–4268, 2020.
- [70] J. Haidar-Ahmad, N. Khairallah, and Z. Kassas, "A hybrid analytical-machine learning approach for LEO satellite orbit prediction," in *Proceedings of International Conference on Information Fusion*, 2022, pp. 1–7.
- [71] M. Orabi, J. Khalife, and Z. Kassas, "Opportunistic navigation with Doppler measurements from Iridium Next and Orbcomm LEO satellites," in *Proceedings of IEEE Aerospace Conference*, March 2021, pp. 1–9.
- [72] M. Neinavaie, J. Khalife, and Z. Kassas, "Acquisition, Doppler tracking, and positioning with Starlink LEO satellites: First results," *IEEE Transactions on Aerospace and Electronic Systems*, vol. 58, no. 3, pp. 2606–2610, June 2022.
- [73] T. Mortlock and Z. Kassas, "Performance analysis of simultaneous tracking and navigation with LEO satellites," in *Proceedings of ION GNSS Conference*, September 2020, pp. 2416–2429.
- [74] J. Farrell and M. Barth, *The Global Positioning System and Inertial Navigation*. New York: McGraw-Hill, 1998.
- [75] B. Tapley, M. Watkins, C. Ries, W. Davis, R. Eanes, S. Poole, H. Rim, B. Schutz, C. Shum, R. Nerem, F. Lerch, J. Marshall, S. Klosko, N. Pavlis, and R. Williamson, "The Joint Gravity Model 3," *Journal of Geophysical Research*, vol. 101, no. B12, pp. 28 029–28 049, December 1996.
- [76] J. Vinti, *Orbital and Celestial Mechanics*. American Institute of Aeronautics and Astronautics, 1998.
- [77] X. Tian, G. Chen, E. Blasch, K. Pham, and Y. Bar-Shalom, "Comparison of three approximate kinematic models for space object tracking," in *Proceedings of International Conference on Information Fusion*, 2013, pp. 1005–1012.
- [78] J. Morales, J. Khalife, U. Santa Cruz, and Z. Kassas, "Orbit modeling for simultaneous tracking and navigation using LEO satellite signals," in *Proceedings of ION GNSS Conference*, September 2019, pp. 2090–2099.
- [79] R. Brown and P. Hwang, *Introduction to Random Signals and Applied Kalman Filtering with Matlab Exercises*, 4th ed. John Wiley & Sons, 2012.
- [80] A. Thompson, J. Moran, and G. Swenson, *Interferometry and Synthesis in Radio Astronomy*, 2nd ed. John Wiley & Sons, 2001.
- [81] C. Pinell, "Receiver architectures for positioning with low Earth orbit satellite signals," Master's thesis, Lulea University of Technology, School of Electrical Engineering, Sweden, 2021.
- [82] M. Neinavaie, J. Khalife, and Z. Kassas, "Doppler stretch estimation with application to tracking Globalstar satellite signals," in *Proceedings of IEEE Military Communications Conference*, November 2021, pp. 647–651.
- [83] M. Neinavaie, J. Khalife, and Z. Kassas, "Cognitive opportunistic navigation in private networks with 5G signals and beyond," *IEEE Journal of Selected Topics in Signal Processing*, vol. 16, no. 1, pp. 129–143, 2022.
- [84] F. Farhangian and R. Landry, "Multi-constellation software-defined receiver for Doppler positioning with LEO satellites," *Sensors*, vol. 20, no. 20, pp. 5866–5883, October 2020.
- [85] J. Khalife, M. Neinavaie, and Z. Kassas, "The first carrier phase tracking and positioning results with Starlink LEO satellite signals," *IEEE Transactions on Aerospace and Electronic Systems*, vol. 56, no. 2, pp. 1487–1491, April 2022.
- [86] M. Neinavaie, J. Khalife, and Z. Kassas, "Blind opportunistic navigation: Cognitive deciphering of partially known signals of opportunity," in *Proceedings of ION GNSS Conference*, September 2020, pp. 2748–2757.
- [87] M. Neinavaie, J. Khalife, and Z. Kassas, "Exploiting Starlink signals for navigation: first results," in *Proceedings of ION GNSS Conference*, September 2021, pp. 2766–2773.
- [88] P. Misra and P. Enge, *Global Positioning System: Signals, Measurements, and Performance*, 2nd ed. Ganga-Jamuna Press, 2010.
- [89] P. Groves, *Principles of GNSS, Inertial, and Multisensor Integrated Navigation Systems*, 2nd ed. Artech House, 2013.
- [90] J. Morales and Z. Kassas, "Stochastic observability and uncertainty characterization in simultaneous receiver and transmitter localization," *IEEE Transactions on Aerospace and Electronic Systems*, vol. 55, no. 2, pp. 1021–1031, April 2019.
- [91] N. Khairallah and Z. Kassas, "An interacting multiple model estimator of LEO satellite clocks for improved positioning," in *Proceedings of IEEE Vehicular Technology Conference*, 2022, pp. 1–5.
- [92] J. Morales, J. Khalife, and Z. Kassas, "Opportunity for accuracy," *GPS World Magazine*, vol. 27, no. 3, pp. 22–29, March 2016.
- [93] Z. Kassas and T. Humphreys, "Receding horizon trajectory optimization in opportunistic navigation environments," *IEEE Transactions on Aerospace and Electronic Systems*, vol. 51, no. 2, pp. 866–877, April 2015.
- [94] Z. Kassas, A. Arapostathis, and T. Humphreys, "Greedy motion planning for simultaneous signal landscape mapping and receiver localization," *IEEE Journal of Selected Topics in Signal Processing*, vol. 9, no. 2, pp. 247–258, March 2015.



**Zaher (Zak) M. Kassas** is a professor at The Ohio State University and director of the Autonomous Systems Perception, Intelligence, and Navigation (ASPIN) Laboratory. He is also director of the U.S. Department of Transportation Center: CAR-MEN (Center for Automated Vehicle Research with Multimodal Assured Navigation), focusing on navigation resiliency and security of highly automated transportation systems. He received a B.E. in Electrical Engineering from the Lebanese American University, an M.S. in Electrical and Computer Engineering from The Ohio State University, and an M.S.E. in Aerospace Engineering and a Ph.D. in Electrical and Computer Engineering from The University of Texas at Austin. He is a recipient of the 2018 National Science Foundation (NSF) Faculty Early Career Development Program (CAREER) award, 2019 Office of Naval Research (ONR) Young Investigator Program (YIP) award, 2022 Air Force Office of Scientific Research (AFOSR) YIP award, 2018 IEEE Walter Fried Award, 2018 Institute of Navigation (ION) Samuel Burka Award, and 2019 ION Col. Thomas Thurlow Award. He is an Associate Editor of the IEEE Transactions on Aerospace and Electronic Systems and the IEEE Transactions on Intelligent Transportation Systems. He is a Fellow of the ION and a Distinguished Lecturer of the IEEE Aerospace and Electronic System Society. His research interests include cyber-physical systems, estimation theory, navigation systems, autonomous vehicles, and intelligent transportation systems.



**Nadim Khairallah** received his M.S. in Mechanical and Aerospace Engineering from the University of California, Irvine and B.E. in Mechanical Engineering with High Distinction from the American University of Beirut. He was a member of the Autonomous Systems Perception, Intelligence, and Navigation (ASPIN) Laboratory. He is a recipient of the 2022 IEEE Vehicular Technology Conference best student paper award. He is currently a guidance, navigation, and control engineer at SpaceX. His research interests include satellite-based opportunistic

navigation, sensor fusion, and estimation theory.



**Sharbel Kozhaya** is a Ph.D. student at The Ohio State University and a member of the Autonomous Systems Perception, Intelligence, and Navigation (ASPIN) Laboratory. He received a B.E. in Electrical Engineering from the Lebanese American University. His current research interests include opportunistic navigation, cognitive software-defined radio, and low Earth orbit satellites.